Justification for 20 Years Inspection Interval for Reactor Coolant Pump Flywheel

Non-Proprietary Version

July 2009

Revision History

Revision	Page	Description
0	All	Original Issue

Mitsubishi Heavy Industries, Ltd.
16-5, Konan 2-chome, Minato-ku
Tokyo 108-8215 Japan

Abstract

The purpose of this document is to present the results of an analysis of the US-APWR Reactor Coolant Pump (RCP) Flywheel integrity which is intended to provide justification for extending the in-service inspection (ISI) interval from the Regulatory Guide (RG) 1.14 required 40 months. The study contained in this report is based on probabilistic fracture mechanics (PFM) to determine the influence of ISI interval on the failure probability of RCP Flywheel.

This report describes the development of a software tool (FRAISE Code) and the following features contained in the Code:

- Stress and stress intensity factor
- Crack size, fatigue crack growth rate
- Fracture toughness, tensile properties and RT_{NDT}
- Monte Carlo simulation

This report provides a comparison of the probability of failure of the RCP flywheel based on a 3 year (~40 month) and a 20 year inspection interval.

The results of the evaluation indicate that the increased risk due to failure of the flywheel with the 20 years inspection interval is negligibly small. Hence, a 20 year inspection interval following the pre-service inspection (PSI) is justified in lieu of the inspection requirement in RG 1.14.

Table of Contents

List of Tables

List of Figures

List of Figures (Cont'd)

List of Acronyms

The following list defines the acronyms used in this document.

ASME	**American Society of Mechanical Engineers**
ISI	**In-Service Inspection**
MHI	**Mitsubishi Heavy Industries, Ltd.**
NRC	**U.S. Nuclear Regulatory Commission**
RCP	**Reactor Coolant Pump**
RG	**Regulatory Guide**
PFM	**Probabilistic Fracture Mechanics**
PNNL	**Pacific Northwest National Laboratory**
PSI	**Pre-Service Inspection**
PT	**Penetrant Test**
SAW	**Submerged Arc Weld**

1.0 INTRODUCTION

The US-APWR reactor coolant pump (RCP) flywheels are quite large and operate at very high speeds. In the unlikely event of a failure, they pose a potential safety concern to the reactor coolant system, the containment and other equipment or systems important to safety as a result of the effects of the resulting missile impact. Regulatory Guide 1.14 (RG 1.14), Revision 1 (Reference 1), presents a methodology for minimizing the potential for failure of the RCP flywheels. The RG 1.14 (Reference 1) provides the material, fabrication, design, testing and inspection requirements necessary to assure safe operation of the RCP flywheel while in service. One of requirements in RG 1.14 (Reference 1) is to perform an in-place ultrasonic volumetric examination every 40 months on the areas of high stress concentrations at the bore and keyway of the RCP flywheel. These examinations should be performed during refueling or maintenance outages coinciding with the in-service inspection (ISI) schedule, as required by American Society of Mechanical Engineers (ASME) Code, Section XI (Reference 2). In addition, surface examination of all exposed surfaces and complete ultrasonic volumetric examination are required at an approximately 10 year interval, during the plant shutdown, coinciding with the ISI schedule, as required by ASME Code, Section XI (Reference 2).

The RCP flywheel inspections, both at the 40 month and the 10 year intervals, have resulted in significant outage time, man-rem exposure and cost to utilities which may be minimized by use of a more carefully designed inspection program. As such, several utilities have performed studies to provide justification for an alternate inspection interval (References 3, 4). These studies, based on deterministic fracture mechanics approach, concluded that an inspection interval greater than 40 years could easily be justified, but in the safety evaluation, the NRC granted a 10 year interval to coincide with the inspection interval for Class 1 components in ASME Code, Section XI (Reference 2). However, recent experience has shown that the currently approved 10 year interval does not coincide with the actual RCP refurbishment schedule at many plants, hence imposing unnecessary hardship for the inspection of the RCP flywheel.

The purpose of this document is to describe the results of a study of the influence of ISI on the failure probability of RCP flywheels designed by Mitsubishi Heavy Industries (MHI) for use in the US-APWR. These results should be useful in establishing an inspection schedule that provides a minimum of cost and radiation exposure consistent with high component reliability. Regulatory Guide 1.14 (Reference 1) requires that inspections be performed every 40 months. This study will justify an inspection interval of at least 20 years by determining the increased risk from a 40 month (~ 3 years) inspection interval to a 20 year inspection interval.

The probabilistic analysis is performed by use of the FRAISE software. FRAISE is an acronym for Flywheel Reliability Analysis In Service Examination and is a computer code for applying PFM to prediction of the probability of failure of a flywheel due to fatigue crack growth from pre-existing defects. The effects of ISI are included through the probability of detecting a crack as a function of its size.

Figure 1-1 shows the various components of the FRAISE code and their inter-relationships.

The overall geometry of the RCP flywheel is shown in Figure 1-2, with details of the keyway area shown in Figures 1-3. As shown, the RCP flywheel is composed of two pieces, one of thickness 11.09 inches and the other 4.51 inches. Table 1-1 provides details of the operation of the RCP flywheel.

Table 1-1 Operating Conditions

1. Operating Temperature

RCP Flywheel will be operated in [120] °F.

2. Operating Conditions

RCP Flywheel will be operated as follows;

Flywheel Operating Conditions (In-service life beyond 60years)

Mode	Speed change (min^{-1})	Frequency (times)	Temperature (F)
RCP start	0 → 1200	(	)
RCP stop	1200 → 0		
Overspeed	1200 → 1500		

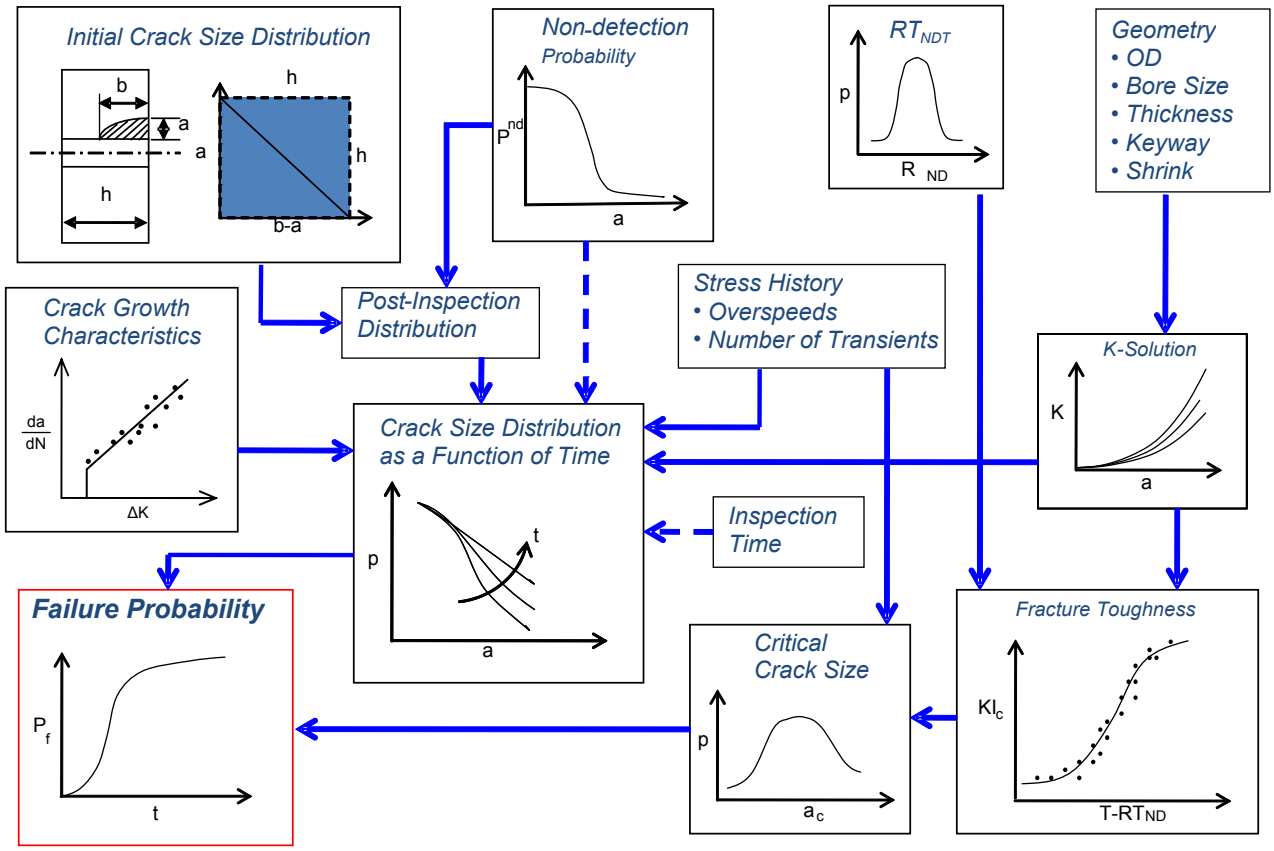

Figure 1-1 Pictorial Representation of the FRAISE Software Showing the Components of the Analysis and Their Relationships

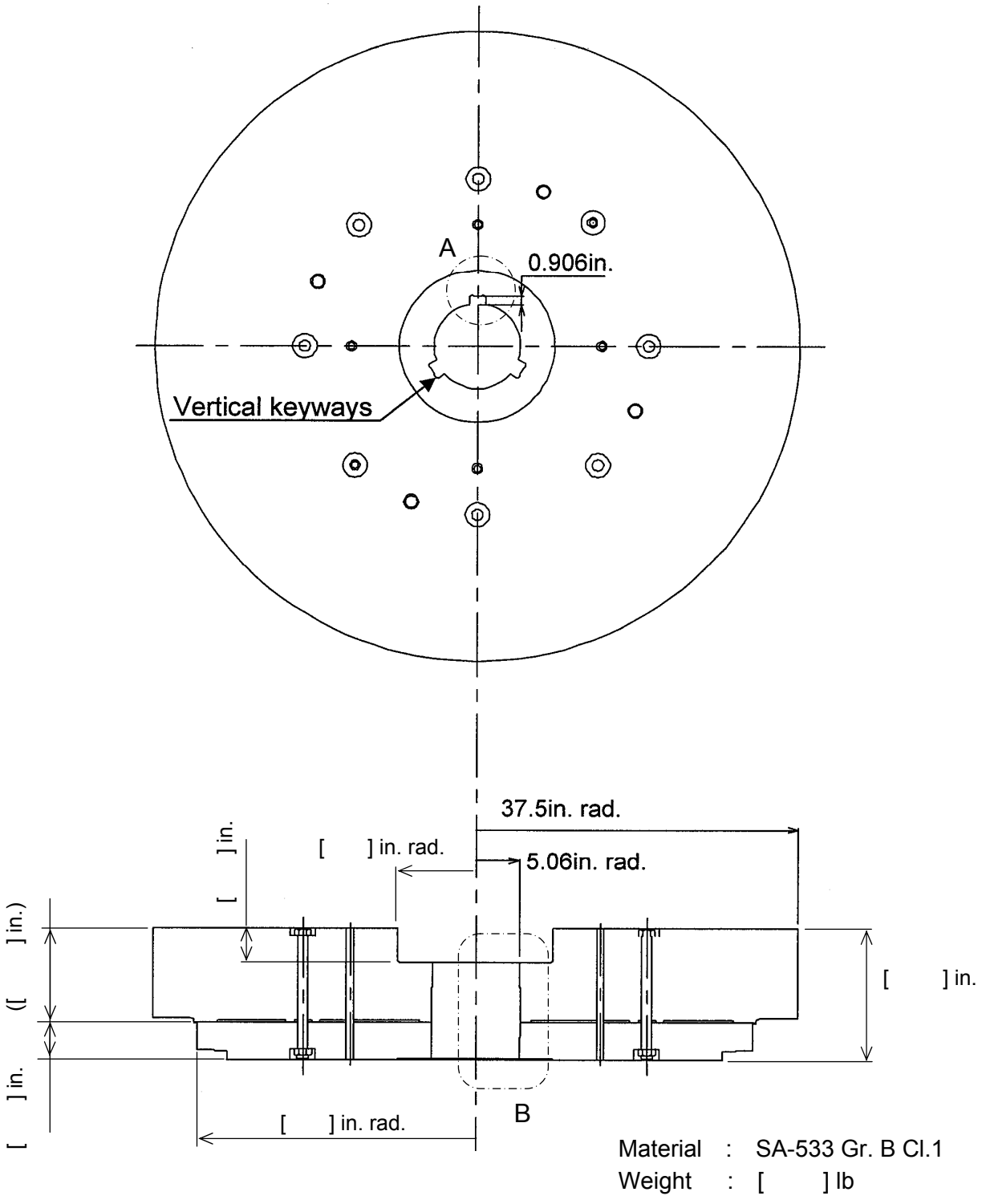

Figure 1-2 Geometry of RCP Flywheel (1/2)

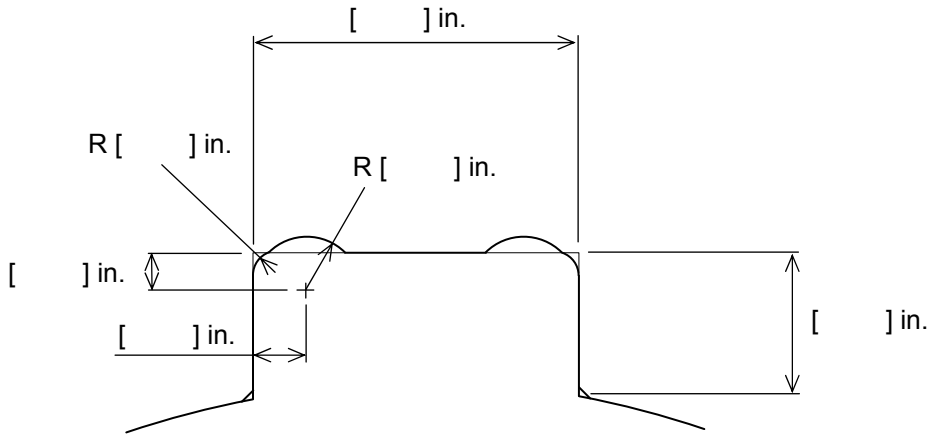

A Detail of Keyway

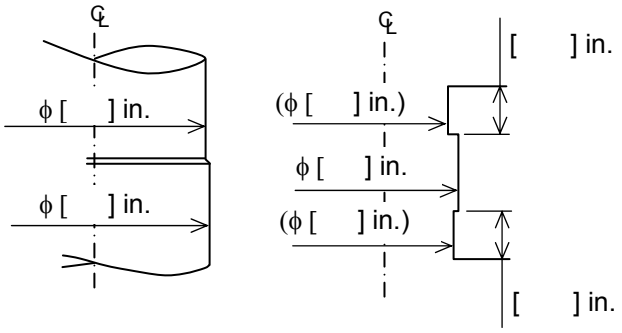

Shrink Fit Range

From 7.87×10^{-4} in. to 1.57×10^{-3} in.

(Average 1.18×10^{-3} in.)

B Detail of Motor Shaft and Flywheel Bore

Figure 1-3 Geometry of RCP Flywheel (2/2)

2.0 STRESSES AND STRESS INTENSITY FACTORS

Nominal stresses in the RCP flywheel were determined by classical elasticity. The effects of the keyway and the step thickness change on stresses in the vicinity of the keyway were determined by finite element computations. Stress intensity factors were determined by the use of influence functions from the literature.

2.1 Stresses

Stresses in the uncracked RCP flywheel with no keyway are first determined to define nominal values of the stresses. This is followed by finite element computations to define the effect of the keyway and the step thickness change.

2.1.1 Nominal Stress

Nominal stresses are determined using classical elasticity solutions (such as Timoshenko, Reference 5). The geometry of the RCP flywheel is shown in Figure 1-2. The RCP flywheel is in two parts that are bolted together. Only the thicker part is considered, because the thinner part has a lower nominal stress due to the lack of a thicker outer portion. The geometry is idealized as shown in Figure 2-1, which also shows dimensions from Figure 1-2.

In order to use the classical solution for a spinning disk, the RCP flywheel is further idealized as having a constant thickness, *h*, with the actual inside and outside radius, but with the density adjusted so that the RCP flywheel has the same mass as the RCP flywheel with the step in thickness. This provides the following expression for the effective density

$$\rho_{eff} = \rho \frac{(r_1^2 - r_{in}^2)h + (r_o^2 - r_1^2)h_1}{(r_o^2 - r_{in}^2)h} \tag{2-1}$$

Timoshenko (Reference 5) provides the following equation for the maximum hoop stress, which occurs at the inner radius

$$\sigma_{\theta o} = \frac{3+\nu}{4}\rho_{eff}\omega^2\left[r_o^2 + \frac{1-\nu}{3+\nu}r_{in}^2\right] \tag{2-2}$$

This is the nominal stress for centrifugal loading. Using the Poisson's ratio *v*=0.3 and a density of 0.000733 lb-sec^2/in (0.283 lb/in^3), along with the dimensions given in Figure 2-1, the nominal stress at 1200 RPM (125.6 radians/sec) for a steel flywheel is 20.84 ksi.

Timoshenko (Reference 5) can also be used to estimate the maximum hoop stress in a disk of large outer radius that has an interference fit onto a much smaller shaft. Taking $(r_o^2-r_{in}^2)/(r_o^2+r_{in}^2) \sim 1$, the following expression is obtained for the maximum hoop stress at the inner radius of the RCP flywheel.

$$\sigma_{fit} = \frac{E\delta}{2r_{in}} \tag{2-3}$$

This will be used as the nominal stress for a shrink fit.

Using E=28,920 ksi at [ ] ºF and 2δ=0.00118 inch as the difference of diameter from Figure 1-3, the nominal stress for this fit for a steel flywheel in 1.686 ksi.

2.1.2 Finite Element Stresses

A finite element stress analysis of the uncracked flywheel with the keyway was conducted by use of ANSYS (Reference 6). Figure 2-2 shows the overall model, which is a segment of the RCP flywheel. The analysis was run for properties at [ ] ºF.

Figure 2-3 shows stress contours of the hoop stress at 1200 RPM. The finite element model contained the shaft and incorporated the interference fit. The finite element results showed that the RCP flywheel separated from the shaft at speeds well below 1200 RPM. This was also predicted from classical solutions from Timoshenko (Reference 5), because the radial displacement at the inner surface of the RCP flywheel exceeded the amount of interference fit plus the radial displacement at the outer surface of the shaft. Hence, all the stresses in Figure 2-3 are centrifugal.

Details of the stresses normal to the prospective crack plane emanating from the keyway are included in Table 2-1. The stresses in Table 2-1 are the stresses normal to the prospective crack plane in the finite element model along a line of nodes radially outward from the high stress location. There is some axial variation of the stresses due to the step in thickness, and the maximum stresses are at the free surface on the side where the step is. This is the side shown in Figure 2-3.

2.2 Stress Intensity Factors

Stress intensity factors due to the centrifugal loading and interference fit were determined for through-wall cracks and quarter-elliptical cracks by use of influence functions and the stresses in the uncracked RCP flywheel.

2.2.1 Through-Wall Cracks

Stress intensity factors for through-wall cracks were evaluated using the stresses of Table 2-1 in conjunction with point force solutions (influence functions) for an edge-crack in a half-space (Reference 7) and a buried tunnel crack in an infinite body (Reference 7).

Linear superposition is used along with the point force solution to provide the incremental stress intensity factor for a stress $\sigma(x)$. Integration of the incremental stress intensity factor is used to evaluate the stress intensity factor itself. Linear interpolation between the values of x in Table 2-1 is used to define a continuous stress as a function of x. MATHCAD (Reference 8) provides a convenient way to obtain numerical values of the integral.

The point force solution shown in Figure 2-4 is used for the buried crack. (A corresponding solution is used for the surface crack.)

Linear superposition of the point force solution leads to the following equation for the buried crack tip at $+a$.

$$K = \frac{1}{\sqrt{\pi a}} \int_{-a}^{a} \sigma(x) \sqrt{\frac{a+x}{a-x}} dx \qquad (2\text{-}4)$$

This expression is for the origin of x at the center of the crack. A more convenient expression is obtained by making the change of variable $z=x+a$, which then results in an integral from 0 to $2a$. This provides the expression

$$K = \frac{1}{\sqrt{\pi a}} \int_{0}^{2a} \sigma(z) \sqrt{\frac{z}{2a-z}} dz \qquad (2\text{-}5)$$

For the buried crack, the configuration in Figure 2-5 is considered. The upper part of Figure 2-5 shows a crack emanating from a keyway at a hole. The lower part of the figure shows the corresponding idealized buried crack. The stresses $\sigma(x)$ from Table 2-1 are used with equation 2-5 to estimated K for the crack emanating from the keyway.

Note that the hole and the keyway are represented as a portion of the crack with no stress. The presence of the hole and keyway are not explicitly considered, other than there is no stress over this region of the crack, and the hole and keyway influence the stresses on the portion of the crack emanating from the keyway. The numerical integration was performed using MATHCAD (Reference 8).

Figure 2-6 provides a plot of the stress intensity factors evaluated using these two point force solutions for the two load cases considered.

Figure 2-6 shows that the half space stress intensity factors are always greater than those based on the buried crack, so the half space results will be used for the evaluation regardless of crack length. In actuality, the stress intensity factors would be expected to be closer to the buried crack results as *a* exceeds approximately the hole diameter.

2.2.2 Quarter-Elliptical Cracks

Stress intensity factors for the quarter-elliptical cracks depicted in Figure 2-7 were evaluated using pc-CRACK (Reference 9) which uses an influence function from Zheng (Reference 10). For cracks with *a~0*, results from Raju (Reference 11) were employed. pc-CRACK uses the influence function for the quarter-elliptical corner cracks with the stresses from Table 2-1 to evaluate the stress intensity factors by use of numerical integration. This is all built into the pc-CRACK software.

The stresses from Table 2-1 were input to pc-CRACK, and local stress intensity factors at the *a* (surface) and *b* (keyway) points were evaluated. They were then normalized to provide $K_{a,b} / \left[\sigma_{nom} \sqrt{\pi a}\right]$. Centrifugal loading and the interference fit were analyzed. The results are included in Table 2-2. The crack is modeled as being in a body of constant thickness subjected to the stresses in Table 2-1, which are from the finite element model with a stepped thickness.

Figures 2-8 through 2-11 provide plots of the normalized stress intensity factors of Table 2-2, including the half-space through-cracks considered in Figure 2-6.

Table 2-1 Stress Normal to Crack Plane at 0 and 1200 RPM as a Function of Distance from Key Root (Unit: ksi)

x, in.	0	1200	x, in.	0	1200

Table 2-2: Tabulation of $K/\sigma_{nom}(\pi a)^{1/2}$ for Quarter-Elliptical Cracks (1/2) (Many Entries Correspond to Crack with Have *b>h)*

	centrifugal loading						interference fit					
b/a	1		2		5		1		2		5	
a	*a*	*b*	*a*	*b*	*a*	*b*	*a*	*b*	*A*	*b*	*a*	*b*

Table 2-2: Tabulation of $K/\sigma_{nom}(\pi a)^{1/2}$ for Quarter-Elliptical Cracks (2/2) (Many Entries Correspond to Crack with Have *b>h.*

	centrifugal loading						interference fit					
b/a	1		2		5		1		2		5	
a	*a*	*b*	*a*	*b*	*a*	*b*	*a*	*b*	*A*	*b*	*a*	*b*

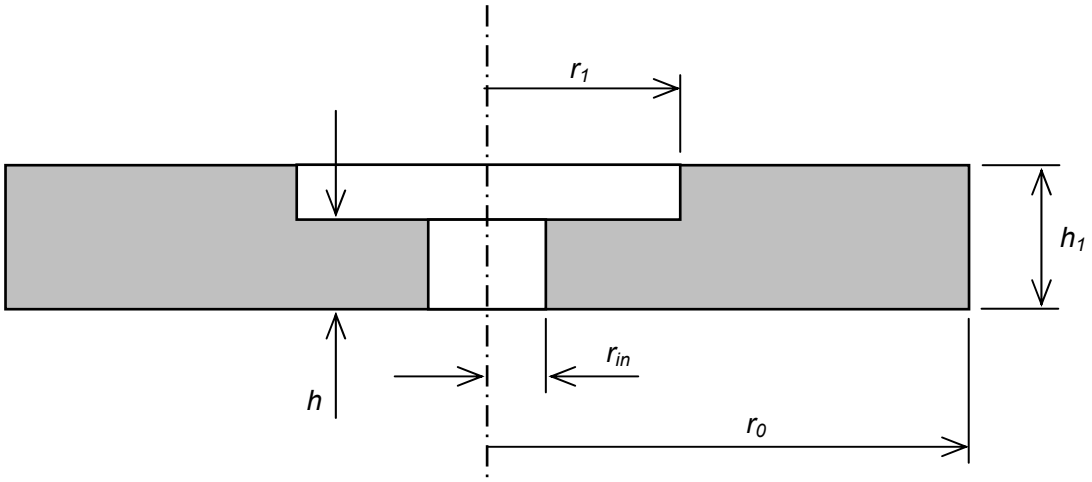

r_{in} = 5.06 h = [ ] Unit : Inches

r_0 = 37.5 h_1 = [ ]

r_1 = [ ]

Figure Idealized Geometry of RCP Flywheel with Dimension as Defined

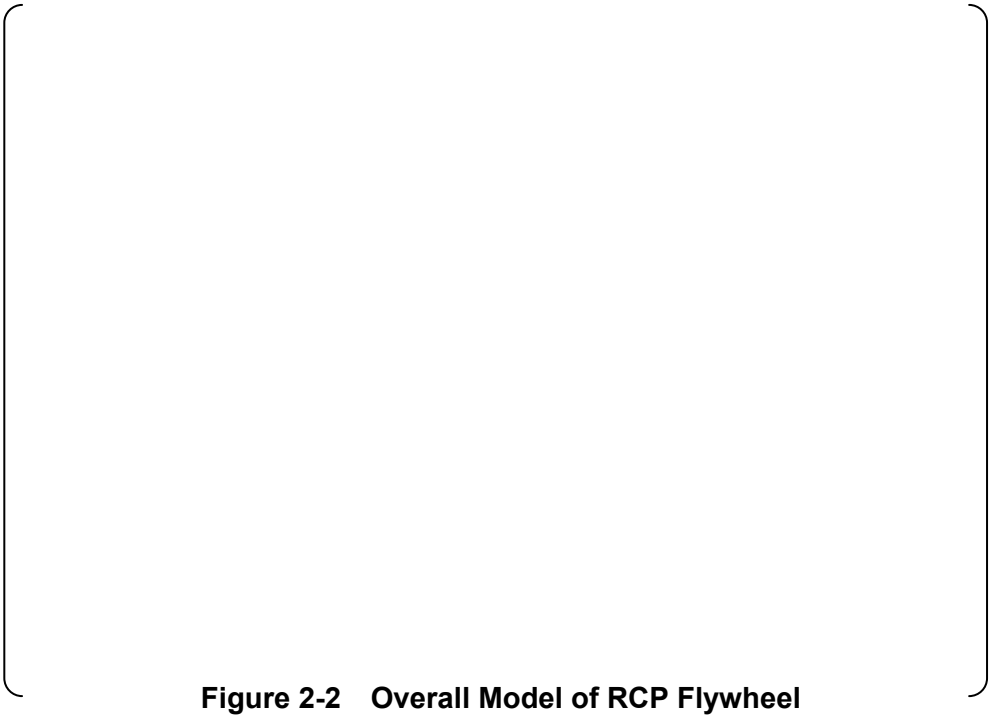

Figure 2-2 Overall Model of RCP Flywheel

Figure 2-3 Details of Centrifugal Hoop Stresses at 1200 RPM

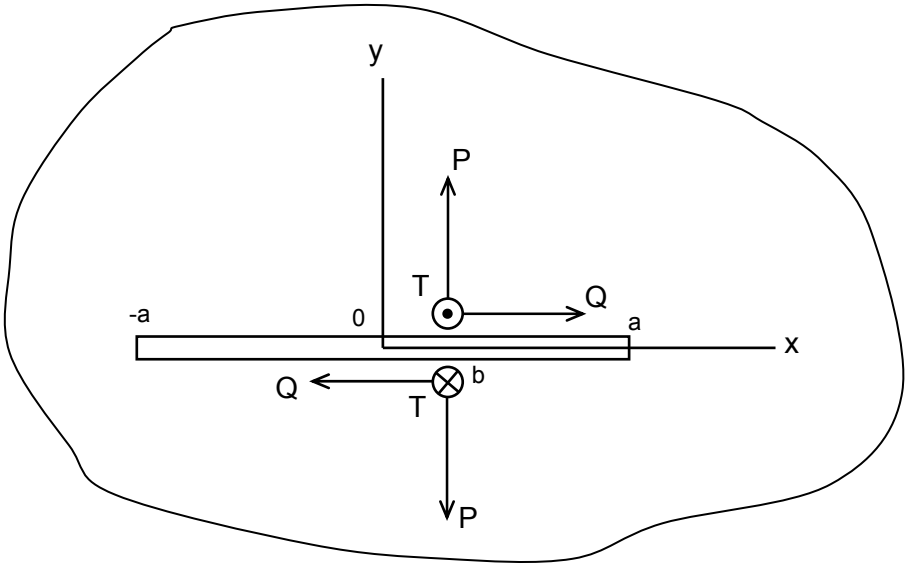

$$\begin{Bmatrix} K_I \\ K_{II} \\ K_{III} \end{Bmatrix}_{\pm\alpha} = \frac{1}{\sqrt{\pi a}} \begin{Bmatrix} P \\ Q \\ T \end{Bmatrix} \sqrt{\frac{a \pm b}{a \mp b}}$$

Figure 2-4 Point Force Solution for a Buried Crack in an Infinite Space

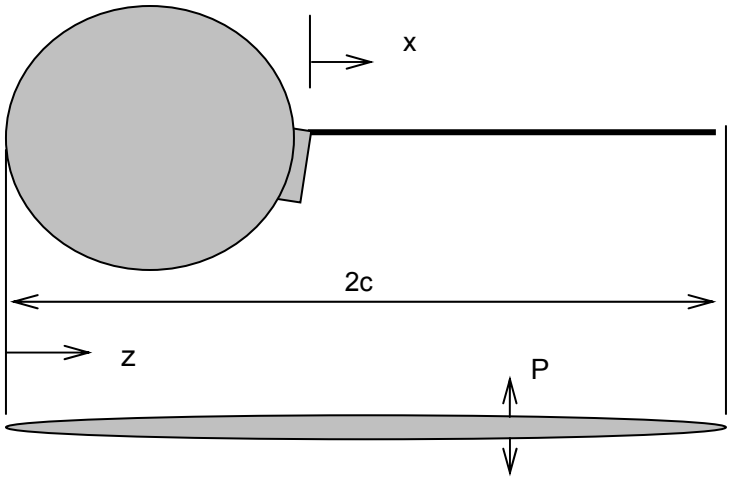

Figure 2-5 Configuration for Evaluation of K for a Buried Crack Using Point Force Solution

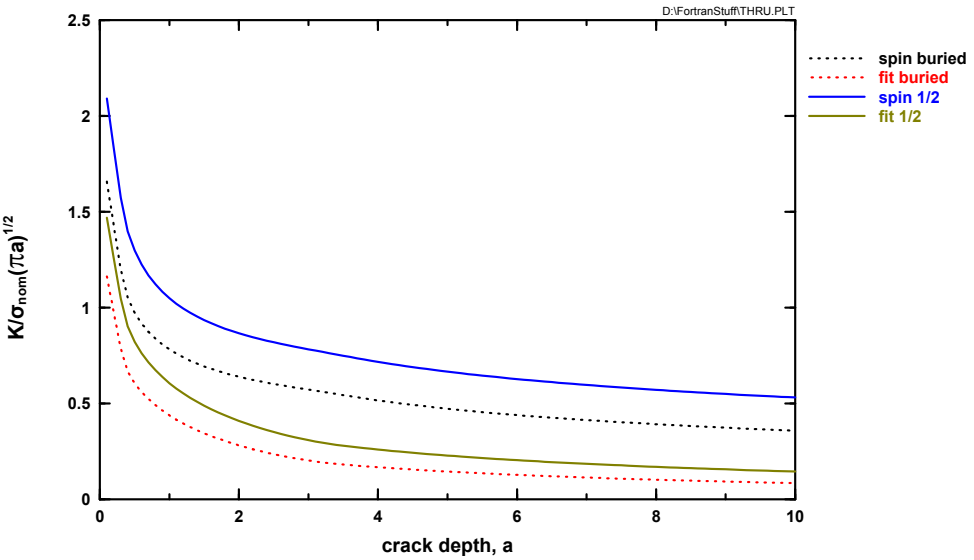

Figure 2-6 $K/\sigma_{nom}\,(\pi a)^{1/2}$ for Centrifugal Loading and Interference Fit as Functions of Crack Depth

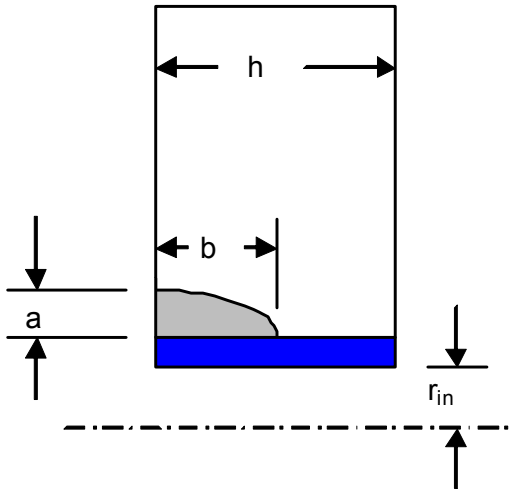

Figure 2-7 Quarter-Elliptical Crack Emanating from the Keyway of a Flywheel

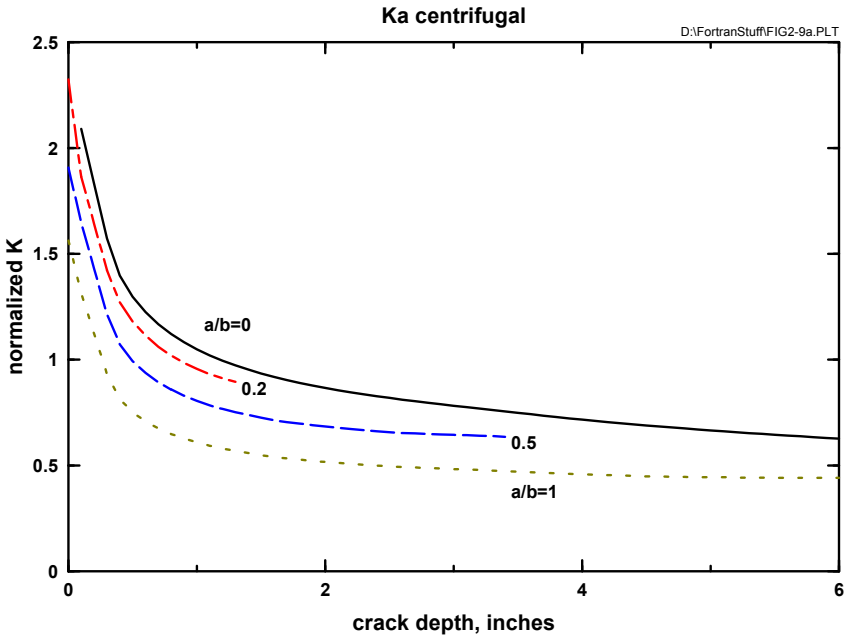

Figure 2-8 $K/\sigma_{nom}\,(\pi a)^{1/2}$ for *a* Direction Centrifugal Loading for Various *a/b*

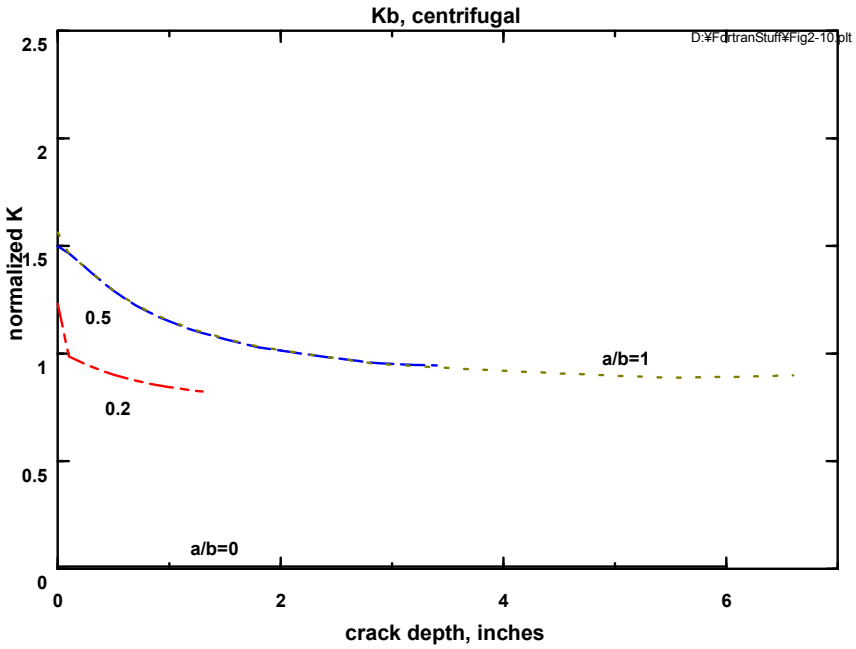

Figure 2-9 $K/\sigma_{nom}\,(\pi a)^{1/2}$ for *b* Direction Centrifugal Loading for Various *a/b*

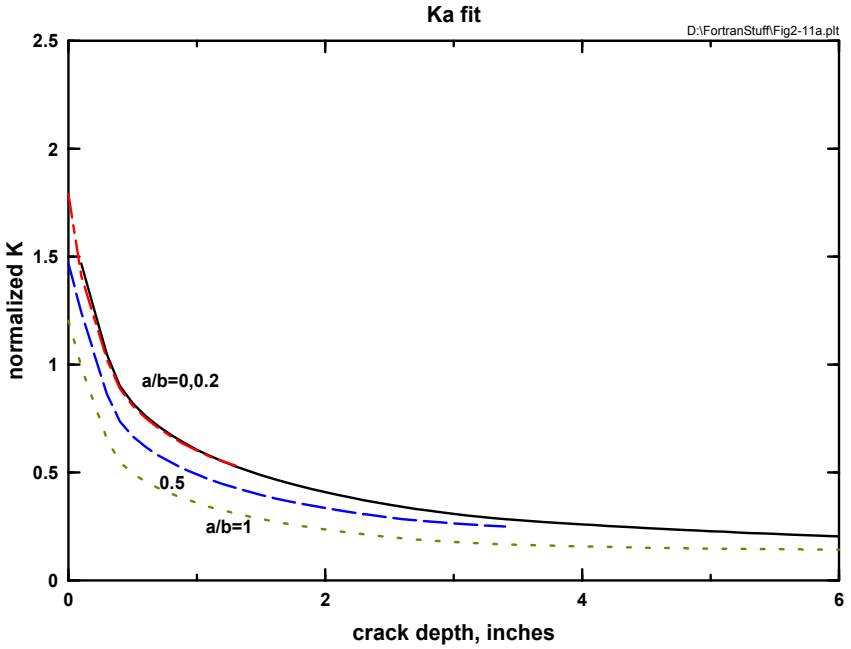

Figure 2-10 $K/\sigma_{nom}\,(\pi a)^{1/2}$ for *a* Direction Interference Fit Loading for Various *a/b*

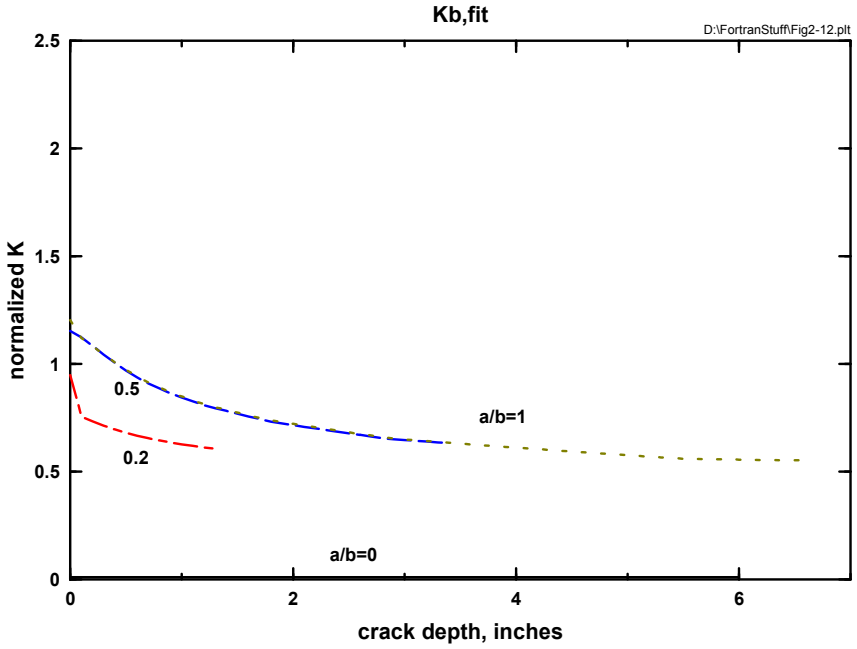

Figure 2-11 $K/\sigma_{nom}\,(\pi a)^{1/2}$ for *b* Direction Interference Fit Loading for Various *a/b*

3.0 CRACK SIZE

Section 2 of this document discussed stress and stress intensity factors, which were dealt with on a deterministic basis. Attention is now turned to description and characterization of the random variables in FRAISE.

The crack size is described by a depth, denoted as *a*, and length, denoted as *b*. The nomenclature of Simonen (Reference 12) will be used. In the context of FRAISE, *a* will be taken as the flaw depth in the radial direction measured from the keyway and *b* is the flaw length in the RCP flywheel thickness direction. The distributions of *a* and *b* will be estimated using information from NUREG/CR-6817 (Reference 12).

Simonen (Reference 12) provide data on the through-wall size and the length minus depth. This is interpreted as applying to elliptical flaws as shown in Figure 3-1.

Figure 3-2 depicts how this crack size is used in FRAISE.

3.1 Crack Depth

Figure 3-3 is a plot of the depth (a_o) distribution of defects, which is Figure 7.2 on page 7.5 of Simonen (Reference 12). Since the RCP flywheel has no welds, base material conditions are of interest. Figure 3-3 shows the Shoreham weld data extending to deepest cracks, and shows the base metal results being parallel to the Shoreham data in the range of depths covered.

The average of base metal will be used, but will be extrapolated to deeper depths by following parallel to the Shoreham weld data. Hence, the Shoreham weld data will be concentrated upon. Extrapolating the Shoreham weld data back to $a = 0$ provides a value of 10^5 flaws per cubic meter. The Shoreham weld data of Figure 3-3 is summarized in Table 3- 1. The flaw numbers are converted to probabilities by dividing by the number at zero ($N_0=10^5$).

The complementary cumulative distribution data of Table 3-1 is plotted on lognormal scales in Figure 3-4.

The line in this figure is the fit to the data as obtained by linear least squares on lognormal probability scales. A good fit to the data is observed, with the parameters of the fit being:

median = a_{50} = [ ] mm = [ ] inch

second parameter = μ = [ ].

3.2 Number of Flaws

The number of flaws per cubic meter must be scaled down from the 10^5 for weld metal to the value appropriate for the average of base metal. From Figure 3-3, an order of magnitude reduction is observed, so that

$N_0 = 10^4/m^3$.

This is a large flaw density. Using the dimensions in Figure 2-1, the volume of material inside the step at r_1 is [ ] m^3, which translates to [ ] flaws. The fracture mechanics analysis within FRAISE considers only one crack, and does not consider crack interactions or crack joining. Consistent with this treatment, FRAISE analysis is performed with one crack drawn directly from the size distributions in Sections 3.1 and 3.3 of this document. This flaw is considered to be present at the keyway with a probability of 1.

3.3 Crack Length

The statistical distribution of initial crack length b_o is also needed. Simonen (Reference 12) assumes an exponential distribution of (b_o-a_o) and evaluates the parameter of the distribution by Bayesian updating using data. This provides a (gamma) distribution of the parameter, and a selected quantile (such as 95%) is then used. As shown in Section 6.2 of Simonen (Reference 12), the data doesn't look very exponential. It is also assumed that (b_o-a_o) and a_o are independent. There is very little data on crack lengths in base metal, and a tight distribution around (b_o-a_o) = 0 is suggested in Simonen (Reference 12). An alternative approach is used here, and it is assumed that the distribution of flaw length is the same as for weld data. This is expected to be conservative, because a much higher percentage of flaws with large length would be expected in a weld as compared to base material. Table 6.10 of Simonen (Reference 12) provides 104 data points of a_o and b_o for Submerged Arc Weld (SAW) in the Shoreham vessel. This data will be employed to define the distribution of (b_o-a_o) for the RCP flywheel material. Figure 3-5 is a plot of the data along with a fit obtained by linear least squares on lognormal scales.

A good fit to the data in Figure 3-5 is observed, suggesting the suitability of a lognormal distribution. The parameters of the distribution are:

median = $(b_o\text{-}a_o)_{50}$ = [ ] mm = [ ] inch

second parameter = μ = [ ]

Using median values, b_o / a_o is [ ], which is certainly conservative.

Table 3-1 Summary of Shoreham Weld Data of Figure 3-3

a, mm	*N(>a)*	*P(>a)*
0	100,000	[
1	30,000	
4	1000	
5	400	
6	200	
7	130	
8	90	
9	60	
10	33	
14	20	]

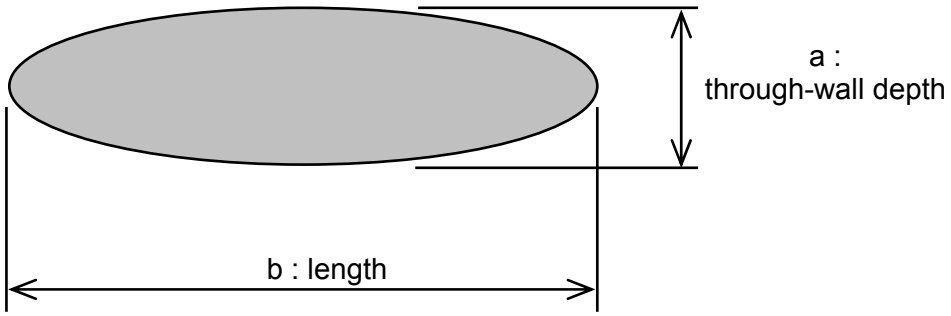

Figure 3-1 Depiction of Buried Crack as Considered in Simonen

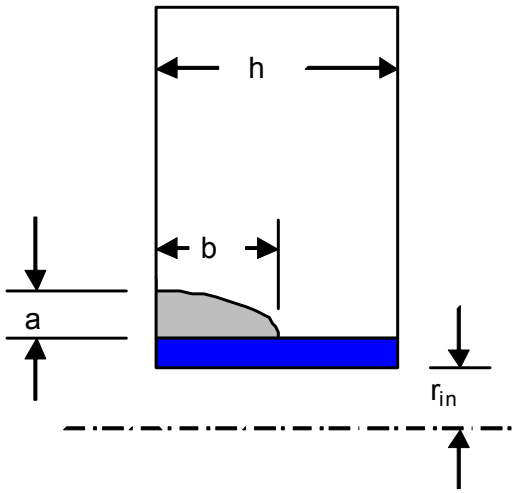

Figure 3-2 Quarter-Elliptical Cracks Considered in FRAISE

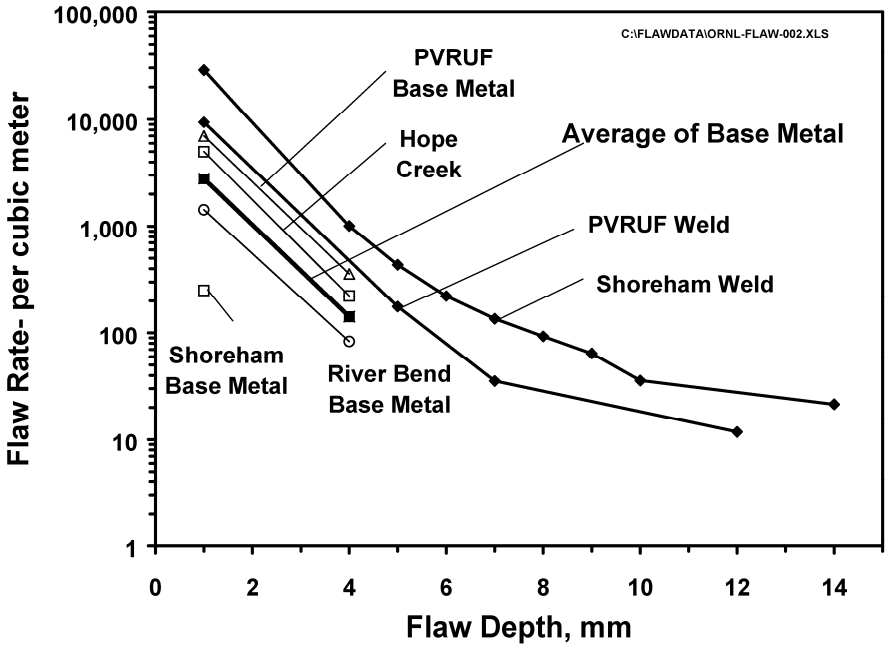

Figure 3-3 Results of Number of Flaws Exceeding a Given Depth for Vessel Materials

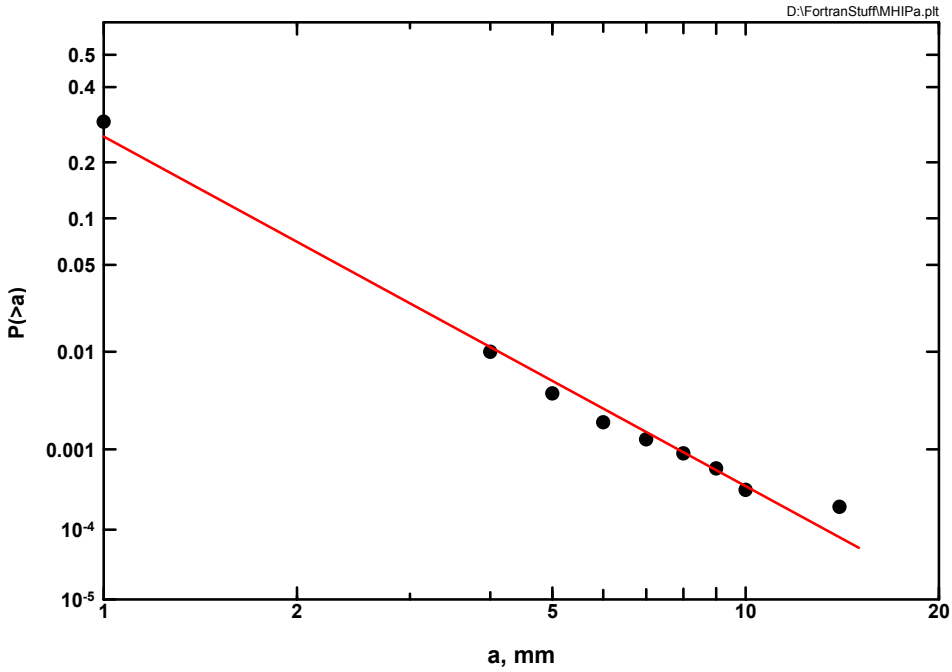

Figure 3-4 Complementary Cumulative Distribution of Crack Depth

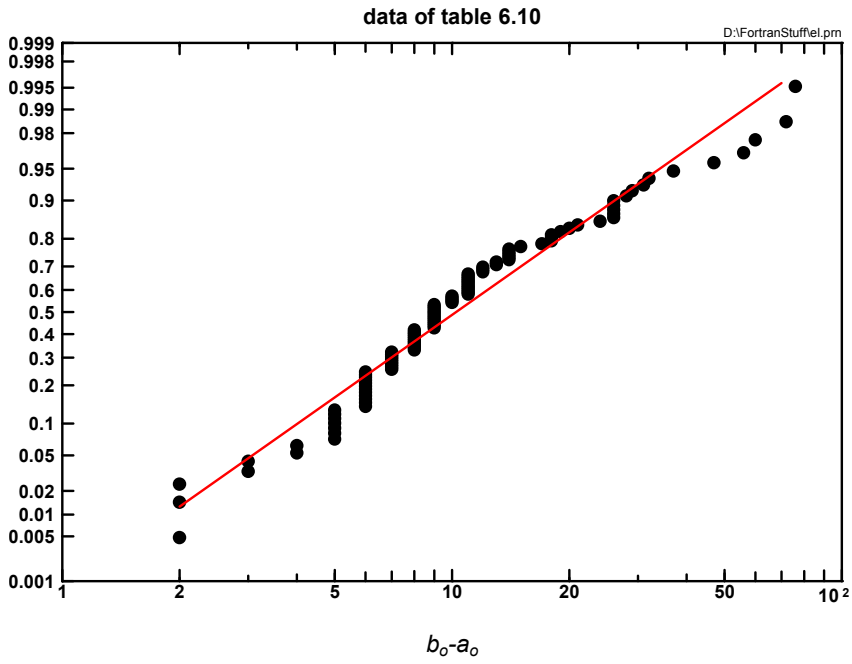

Figure 3-5 Cumulative Distribution of (b_o-a_o) from Data of Simonen on Lognormal Scales with Least Squares for Fit

4.0 FRACTURE TOUGHNESS, TENSILE PROPERTIES AND RT_{NDT}

The statistical distributions of the fracture toughness, tensile properties and RT_{NDT} are characterized in this section.

4.1 Fracture Toughness

The statistical distribution of the fracture toughness for a given excess temperature (T-RT_{NDT}) is given directly in Bass (Reference 13). A three-parameter Weibull distribution is employed, the cumulative distribution of which is given in Equation 4-1. Figure 4-1, which is directly from Bass (Reference 13), is a plot of the data and various quantiles from the fit defined in Equation 4-1

$$P(K_{Ic}) = 1 - e^{-\left[\frac{K_{Ic}-K_0}{b}\right]^c} \quad (4\text{-}1)$$

$$K_o = A_0 + A_1 e^{A_2(T-RT_{NDT})}$$

$$b = B_0 + B_1 e^{B_2(T-RT_{NDT})}$$

$$c = C_0 + C_1 e^{C_2(T-RT_{NDT})}$$

The constants in this fit are given in Table 4-1.

4.2 RT_{NDT}

Data on the RT_{NDT} of SA-533 Grade B Class 1 was obtained from Server (Reference 14) and is included in Table 4-2. This table also includes data on the yield and ultimate strength at room temperature and 550 ºF.

The mean and standard deviation of the RT_{NDT} was computed from the data, and is included at the bottom of Table 4-2. Figure 4-2 provides a plot of the RT_{NDT} data and the corresponding fit on normal probability scales.

The fit is not particularly good, but the normal distribution will be used nonetheless.

4.3 Tensile Properties

The mean and standard deviation of the yield and ultimate strengths are needed for the analysis of ductile failure. Server (Reference 14) provides a comprehensive set of data on 24 heats of SA-533 Grade B Class 1 steel that are used to characterize the statistical distributions of the yield and ultimate strengths at various temperatures. Room temperature and 550 ºF are considered here. Table 4-2 summarizes the information from Server (Reference 14), which also include data on RT_{NDT}. If tensile properties are given in Server (Reference 14) for a temperature between 64 and 75 ºF, then this is used directly for the room temperature entry in Table 4-2. If no direct entry is available, then data from Server (Reference 14) is linearly interpolated to provide a value at 74ºF.

In all cases, data for 550 ºF is included in Server (Reference 14). The “ID” in Table 4-2 is the designation of the heat of the material as identified in Server (Reference 14). If more than one set of tensile properties is given for a particular heat and temperature, then the number in Table 4-2 is the mean of the values.

The lower two rows in Table 4-2 are the mean and standard deviation of the data in the column above. Figures 4-3 and 4-4 provide normal probability plots of the tensile data in Table 4-2 along with the line corresponding to the mean and standard deviation of the data.

Table 4-1 Constants in Fit of Distribution of Fracture Toughness (ksi-in$^{1/2}$, ºF)

	0	1	2
A	10.8957	23.4192	0.0023
B	14.7582	42.6312	0.0124
C	2.03025	0.4983	0.0135

Table 4-2: Tensile and RT_{NDT} Data from Server

		room temperature		550ºF	
ID	RT_{NDT}	yield	ultimate	yield	ultimate
A	5.0	70.42	92.42	61.76	89.95
B	60.8	63.62	85.62	55.20	83.70
C	15.8	65.20	86.20	55.20	81.70
D	10.4	63.90	87.60	58.20	84.70
E	30.2	63.17	86.52	57.70	82.90
F	15.8	65.17	86.30	56.40	84.00
G	-0.4	58.60	81.10	53.11	80.30
H	10.4	65.50	86.60	56.00	82.60
I	-0.4	57.20	81.90	53.10	81.10
J	19.4	53.85	78.15	48.45	77.30
K	-0.4	64.60	87.70	53.90	84.90
L	-9.4	65.70	87.20	60.00	87.10
M	10.4	70.50	93.50	63.50	91.90
N	-0.4	63.40	87.60	57.20	86.60
P	-70.6	70.71	85.09	68.80	83.10
Q	-70.6	70.04	83.50	63.10	83.60
R	-59.8	71.91	85.62	62.40	83.20
S	-79.6	70.15	83.23	59.40	79.78
T	-9.4	70.80	88.00	62.90	84.10
U	-40.0	80.60	91.60	68.80	86.90
V	-70.6	81.97	93.26	72.40	90.20
W	-70.6	77.53	90.78	66.71	82.00
X	-70.6	78.89	88.33	67.00	86.20
Y	-70.6	78.27	91.91	66.70	87.10
mean	-18.6	68.40	87.07	60.3	84.37
std dev	40.4	7.19	3.81	5.92	3.37

temperature in ºF, stress in ksi

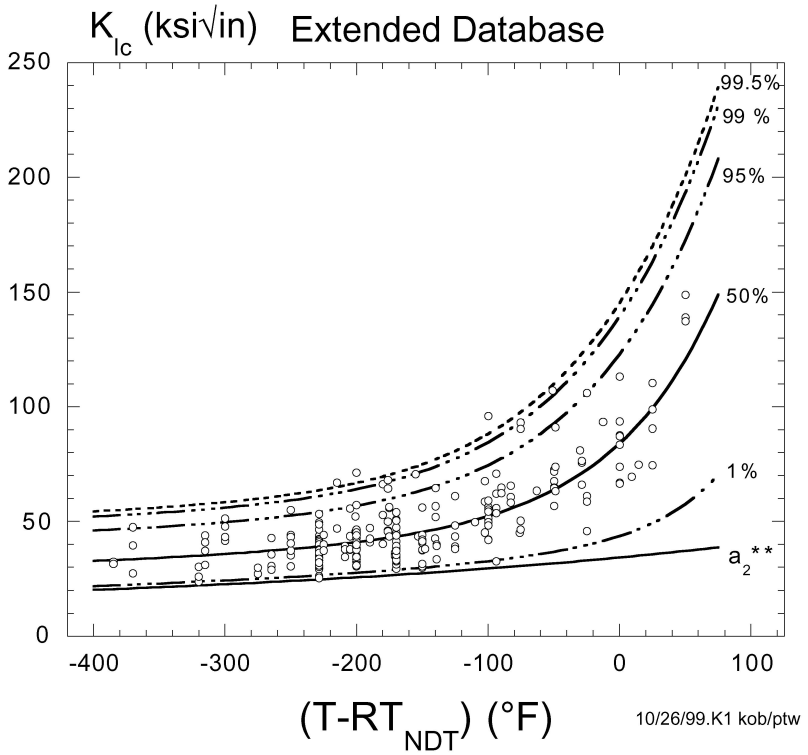

Figure 4-1 Fracture Toughness Data for SA-533 Steel with Plots of Various Quantiles of the Three-Parameter Weibull Fit

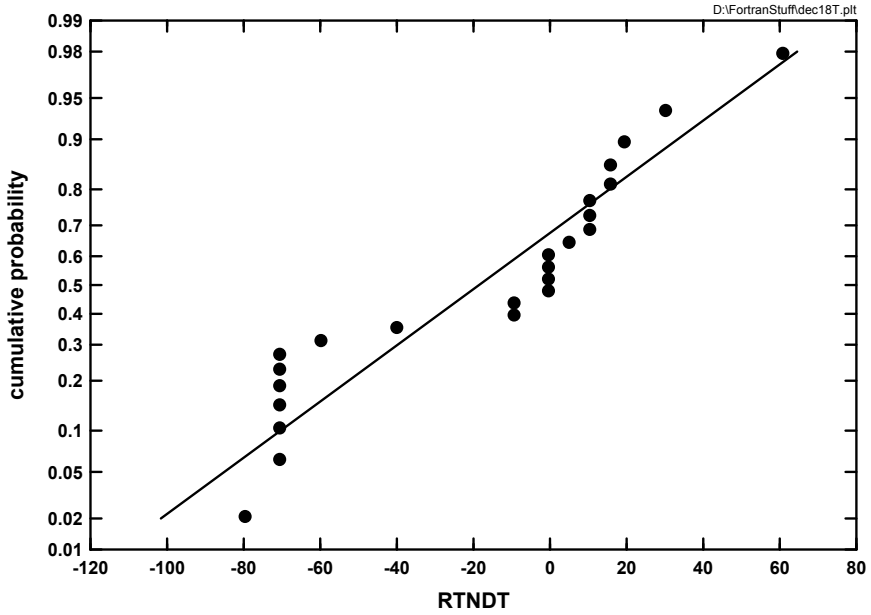

Figure 4-2 Cumulative Distribution of the RT_{NDT} from the Data in Table 4-2

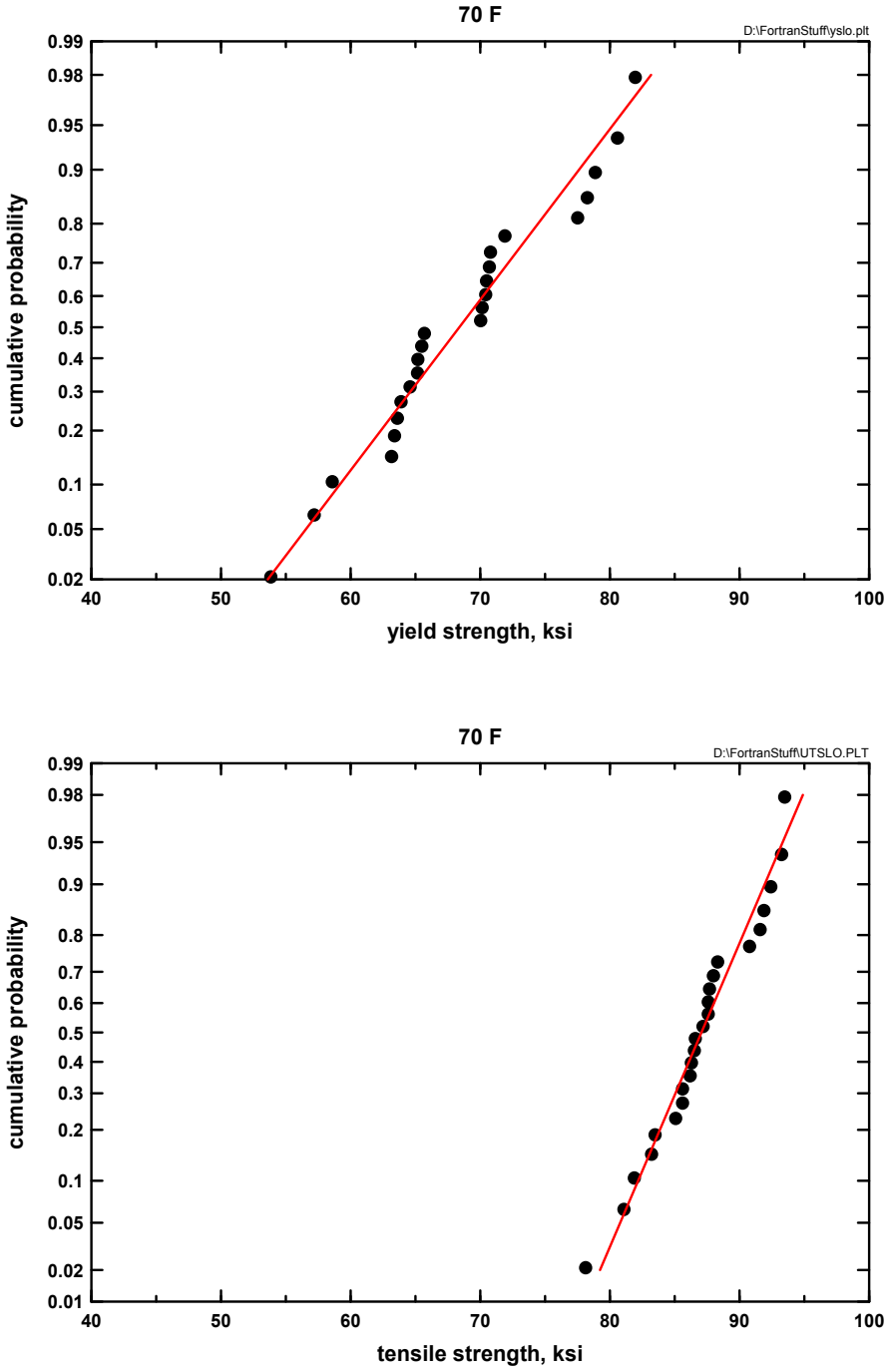

Figure 4-3 Comparisons of Data and Fit for Cumulative Distributions of Yield and Ultimate Strength at Room Temperature

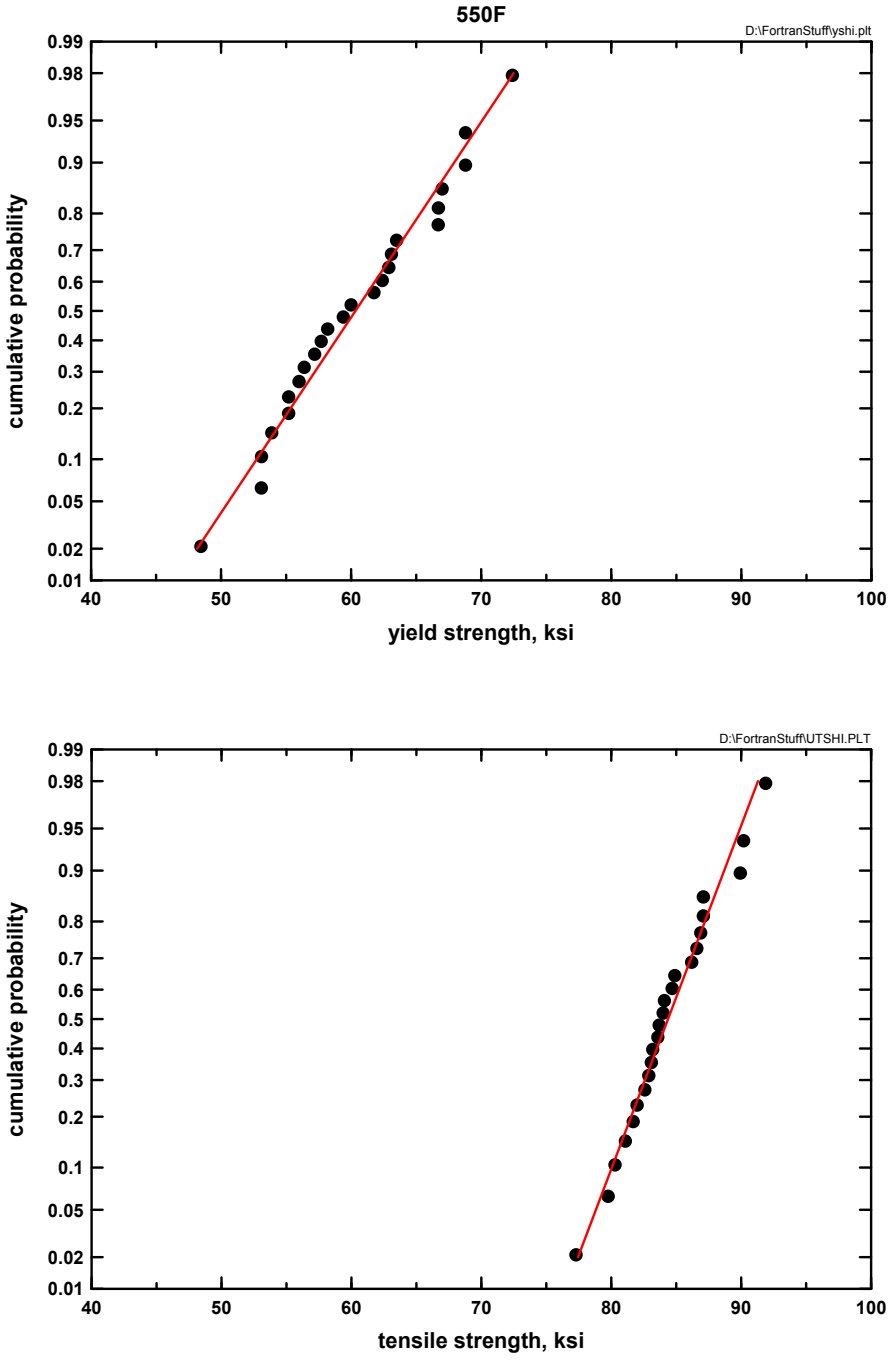

Figure 4-4 Comparisons of Data and Fit for Cumulative Distributions of Yield and Ultimate Strength at 550 ºF

5.0 FATIGUE CRACK GROWTH RATE

Cracks are considered to grow due to cyclic loading. Following the ASME Code, Section XI (Reference 2) and Eason (Reference 15) the fatigue crack growth relation is taken to be

$$\frac{da}{dN} = \begin{cases} C\left[\frac{\Delta K}{2.88 - R}\right]^{3.07} & \Delta K > \Delta K_{th} \\ 0 & \Delta K < \Delta K_{th} \end{cases} \qquad (5\text{-}1)$$

where K_{max} and K_{min} are the maximum and minimum stress intensity factors during a cycle, and $\Delta K = K_{max} - K_{min}$, $R = K_{min}/K_{max}$.

Threshold conditions (ΔK_{th}) are discussed below.

The scatter in fatigue crack growth properties is described by considering *C* to be a random variable with distribution type and parameters defined by fatigue crack growth data. Figure 5-1, which is from Eason (Reference 15) is a plot of a portion of the fatigue crack growth data, compensated to a value of *R* of 0.1.

The 99% bounds on the data are shown, and are stated in Eason (Reference 15) to be related to a lognormal distribution of *C*. The best fit value of *C* is given as 4.14×10^{-9}, when *da/dN* is in inches per cycle and *ΔK* is in ksi-$in^{1/2}$.

Knowing the 99% interval of the data, the median value of *C* and that the distribution is lognormal allows the parameters of the distribution to be evaluated, with the following results:

$C_{50} = 4.14 \times 10^{-9}$ (*da/dN* inches per cycle, *K* ksi-$in^{1/2}$)

$\mu = 0.621$

This characterizes the scatter in the fatigue crack growth rate for a given *ΔK*.

The *ΔK* threshold condition is given in the ASME Code, Section XI (Reference 2) for positive *R* as

$$\Delta K_{th} = 5.0(1 - 0.8R) \text{ ksi-in}^{1/2} \qquad (5\text{-}2)$$

This linear functional form will be used, with the constants evaluated from data from Paris (Reference 16) and Liaw (Reference 17).

Table 5-1 summarizes the data, which includes all entries at 75 and 550 ºF in Table 2 of Paris (Reference 16) and all entries in Table 5 of Liaw (Reference 17). The data includes base metal and weld metal in various grades and classes of SA-533 and SA-508. The fatigue thresholds for the various materials, grades and classes and weld metal vs. base metal appear similar, and all are included to expand the available data base.

The fatigue crack threshold data of Table 5-1 was first fitted by linear least squares to the functional form of Equation 5-2 as suggested in the ASME Code, Section XI (Reference 2).

$$\Delta K_{th} = A - BR \tag{5-3}$$

Values of *A* and *B* were obtained for both temperatures in Table 5-1. This provided the median value of ΔK_{th} as a function of *R* for a given temperature. The distribution of the threshold was assumed to be lognormal, with a constant μ for a given temperature. The value of μ was obtained by maximum likelihood (Reference 18). In this instance, this means finding μ that maximizes the product of the lognormal density function as expressed in Equation 5-4

$$p(x) = \frac{1}{\mu x\sqrt{2\pi}} e^{-\frac{1}{2\mu^2}\left(\ln\frac{x}{x_{50}}\right)^2} \tag{5-4}$$

The expression for the likelihood is

$$L(\mu) = \prod_{n=1}^{ndat} \frac{1}{\mu\sqrt{2}K_n} e^{-\frac{1}{2\mu^2}\left[\ln\left(\frac{A-BR_n}{K_n}\right)\right]^2} \tag{5-5}$$

K_n and R_n are the data points from Table 5-1 (for a given temperature), *ndat* is the number of data points at that temperature, and *A* and *B* are already known from the linear least squares mentioned above. The function *L* was evaluated as a function of μ and the maximum picked out of a table. Figure 5-2 is a plot of *L* for room temperature.

A well defined peak is observed from which a value of μ of 0.118 was obtained. A similar procedure was applied to the 550 ºF data. Table 5-2 summarizes the results.

Figures 5-3 and 5-4 provide plots of the threshold data, along with the median fit and the predicted 10th and 90th percentiles.

The fits are seen to be quite good, with about 20% of the data falling outside the 10-90% band. The width of the band in Figures 5-3 and 5-4 varies with *R* even though μ is independent of *R*. This is consistent with the data, and is a consequence of characteristics of the lognormal distribution. (The width of the band depends on both the median and μ, and the median varies with *R*).

It appears that the data from the two references fall into two categories, with the Paris (Reference 16) data falling consistently below the Liaw (Reference 17) data. Nevertheless, the data of the two sources were combined for the statistical analysis.

The fatigue crack growth equation and related constants are not dependent on temperature. The threshold conditions are dependent on temperature. Threshold results are given above for room temperature and 550 ºF. Linear interpolation will be used if threshold at intermediate temperatures is needed.

Information needed to plot various quantiles of the fatigue crack growth as a function of cyclic stress intensity factor is now available, and Figure 5-5 provides such results. The abrupt "knee" in the curves is consistent with the ASME Code, Section XI (Reference 2).

In order for the plots at various quantiles to not cross, the p th quantile of C is used with the (1-p)th quantile of ΔK_{th}. This is because a high fatigue crack growth rate is associated with a low threshold, as shown in Figure 5-5.

Table 5-1: Fatigue Crack Growth Threshold Data from Paris and Liaw (ksi-in$^{1/2}$)

	room temperature		550ºF	
R	Paris	Liaw	Paris	Liaw
0.1	7.3 6.1		4.3 4.7 4.3	
0.2		6.7 6.4 7.2 6.3 7.3 6.8		5.8 5.8
0.3	5.2		3.4 4.05 3.8	
0.5	4.4 5.1	5.2 5.8 5.2	3.1 3.3 3.2	4.1 4.3 4.6 4.6 4.4
0.7	2.8 2.8	3.9	2.45 3.05 2.85	
0.8	2.75		2.5	
	18 data points	||	20 data points	

Table 5-2: Results of Fits for Threshold Conditions

	Room Temperature	550 ºF
A	7.84	5.25
B	6.18	3.12
μ	0.118	0.160

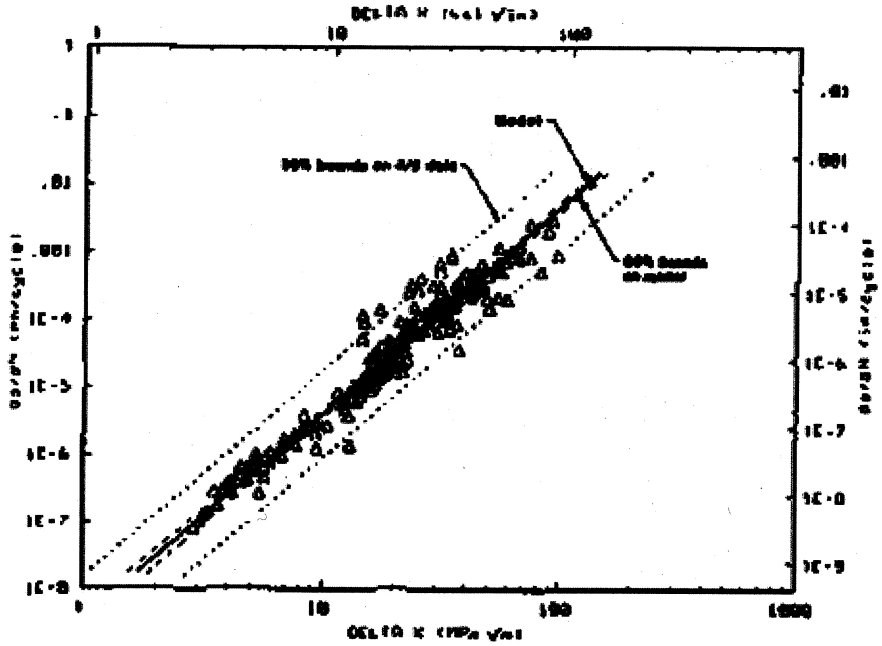

Figure 5-1 Fatigue Crack Growth Rate Data Compensated for R=0.1 Showing 99% Interval of the Data

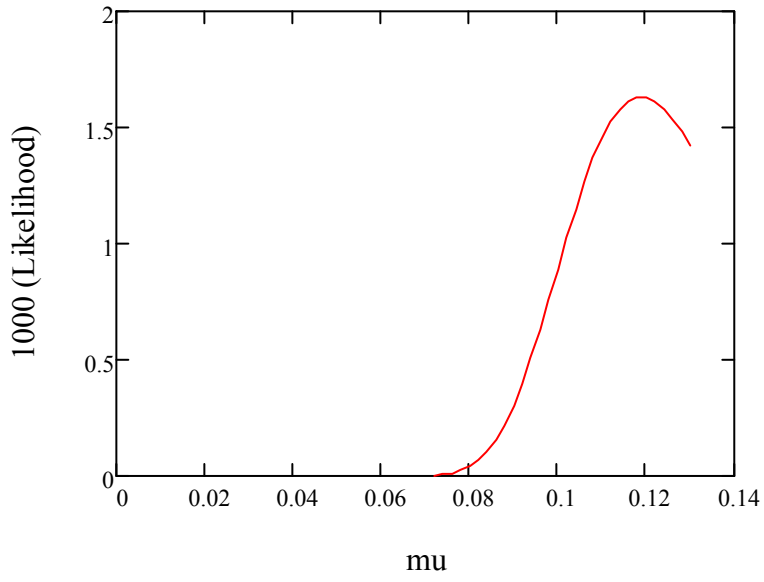

Figure 5-2 Likelihood *L* as a Function of *μ* for Room Temperature Data of Table 5-1

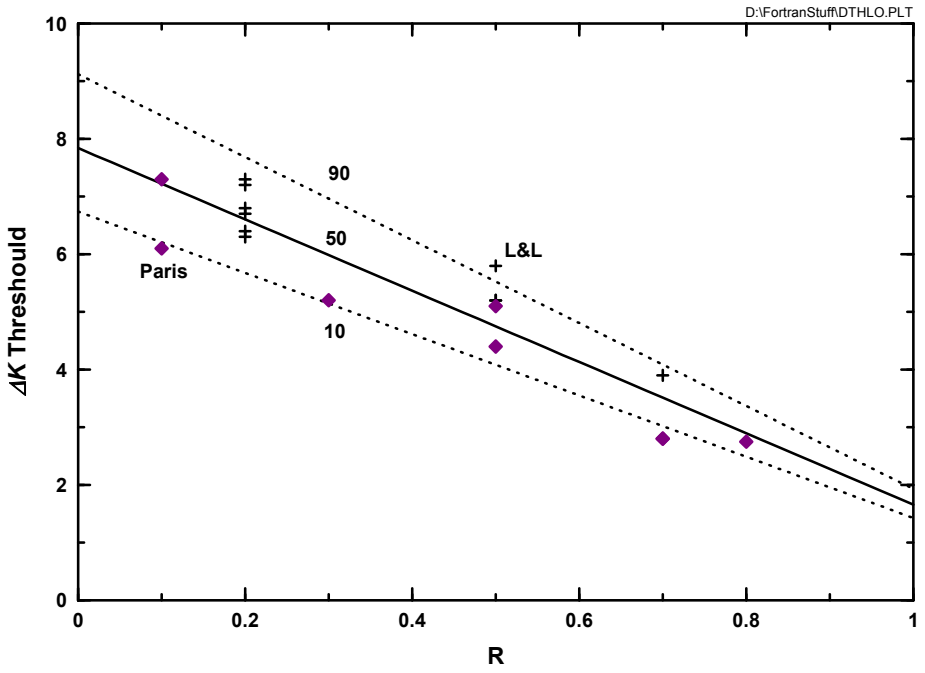

Figure 5-3 *ΔK* Threshold Data Along with Fits of 10th, 50th and 90th Percentiles, Room Temperature

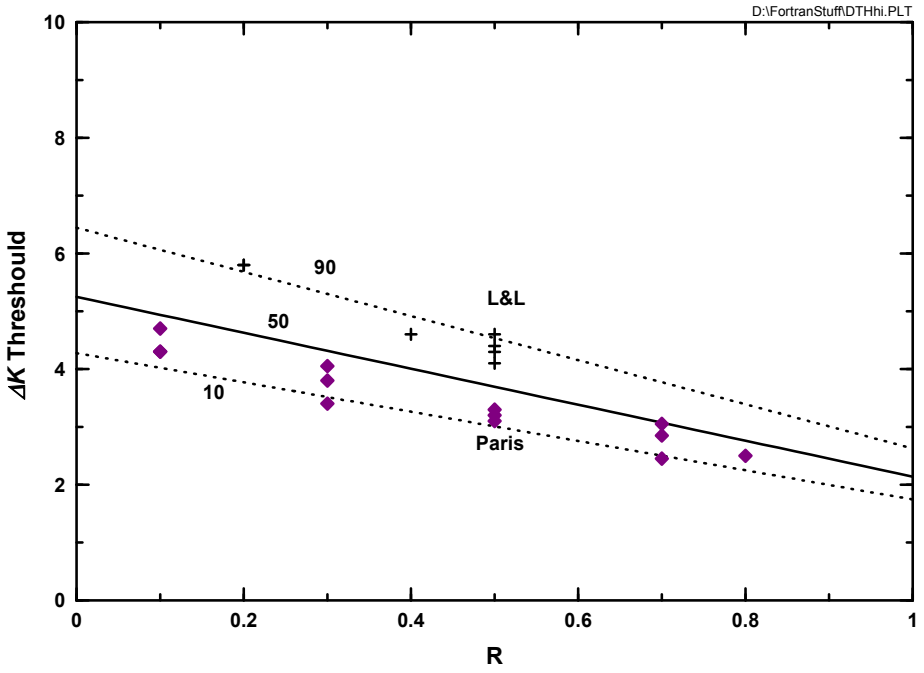

Figure 5-4 *ΔK* Threshold Data Along with Fits of 10th, 50th and 90th Percentiles, 550 ºF

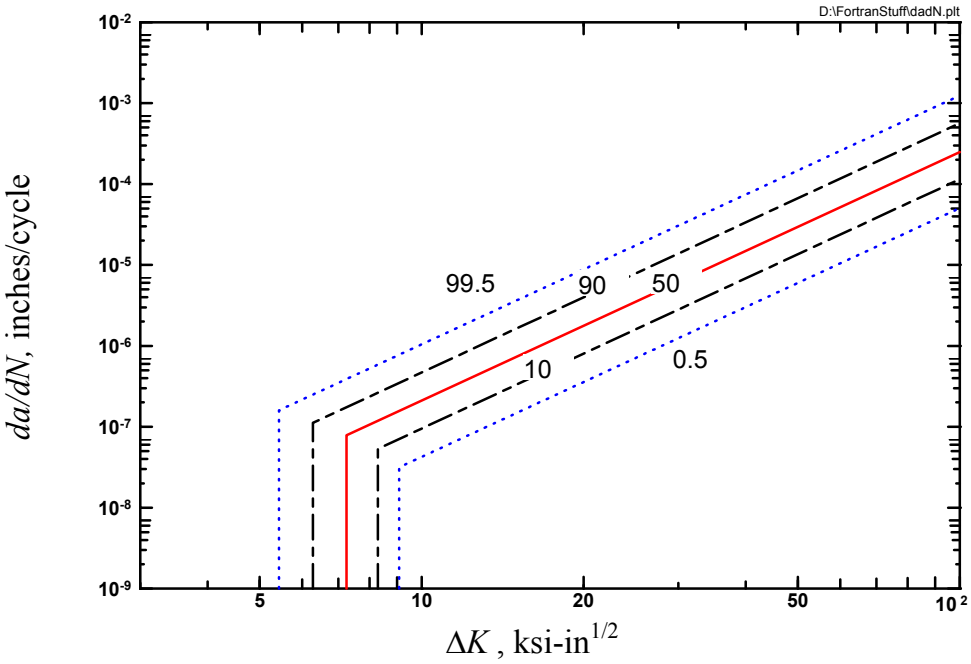

Figure 5-5 Various Quantiles of *da/dN-ΔK* Relation *R* = 0.1, Room Temperature

6.0 CRACK GROWTH AND FINAL FAILURE

The initial cracks are grown using the fatigue crack growth relation and stress history. Growth in the *a* and *b* directions is considered, with the values of *da/dN* and *db/dN* evaluated for each transient using the respective stress intensity factor solution (K_a and K_b as discussed in Section 2).

Once a crack that is initially part-through grows to $b=h$, then the *K* solution transitions to that of a through crack of depth *a*. This transition is shown in Figure 6-1.

Final failure is taken to occur when the maximum stress intensity factor (either K_a or K_b) during any transient results in a *K* that exceeds the value of K_{Ic}. Recall that K_{Ic} itself is a random variable that is influenced by the RT_{NDT} (which is also random).

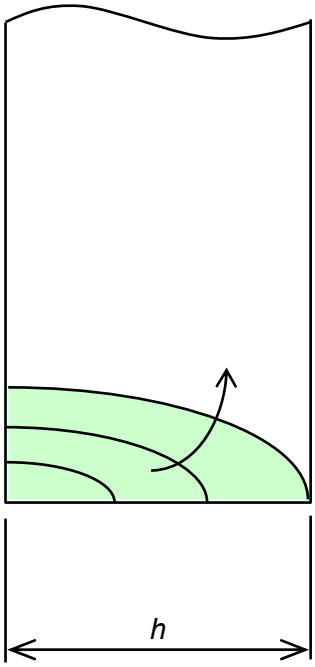

Figure 6-1 Transitioning from a Part-through Crack to Through Crack

7.0 MONTE CARLO SIMULATION

The foundation of FRAISE is a deterministic fracture mechanics analysis that considers crack growth due to cyclic loading, with failure occurring when the maximum stress intensity factor exceeds the fracture toughness of the material. The cyclic loading is due to starts and stops of the RCP flywheel. Pre-existing quarter-elliptical cracks growing out of the high stress region near the keyway are considered. Figure 1-1 provides a pictorial representation of the components of FRAISE and their inter-relationships. Monte Carlo simulation is used to compute the probability of flywheel failure prior to a given time (number of cycles).

7.1 Standard Sampling

The deterministic model provides the lifetime (number of cycles to failure) for a given initial crack size, stress history, fatigue crack growth rate (*da/dn* for a given ΔK), and fracture toughness (which depends on the RT_{NDT}). Some of these inputs to the deterministic calculation of cycles to failure are not precisely known, so are treated as random variables. The probability of failure prior to a given time (number of cycles, *N*) is the probability that a combination of random variables leads to a failure prior to *N*. This probability is evaluated by Monte Carlo simulation, which involves many deterministic calculations of lifetime (trials), each with a set of random variables drawn from their respective distributions. The probability of failure prior to *N*, is simply the fraction of trials that result in a failure prior to *N*. This is expressed as

$$P(N_f < N) = \frac{F}{S} \tag{7-1}$$

F is the number of failures in *S* trials. The effects of inspection alter this somewhat, as discussed in Section 6.3.

Table 7-1 shows a summary of the random variables and Table 7-2 summarizes characteristics of the distributions of random variables considered in FRAISE.

Only the cumulative distribution is given for the three-parameter Weibull, from which the other information can be derived if desired.

The cumulative distribution for the normal and lognormal are written in terms of the complementary error function, which is tabulated in Abramowitz (Reference 19), and is defined as

$$\operatorname{erfc}(x) = \frac{2}{\sqrt{\pi}} \int_x^\infty e^{-t^2}\, dt \tag{7-2}$$

Convenient rational approximation to erfc(x) are provided in Equation 7.1.25 and succeeding equations in Abramowitz (Reference 19).

All of the random variables other than those related to crack size are sampled directly from their distributions. Crack size is a very important in fatigue crack growth analysis, and it is likely that quite large (and low probability) initial cracks will be required to have failures within the [ ] cycle lifetime (see Table 1-1). In order to sample the larger cracks expected to be needed to lead to failure, stratified sampling of crack size is employed. If stratification was not used, then the vast majority of sampled cracks would not lead to failure in the lifetime. Such stratification of crack size was employed in PRAISE (Reference 20, 21, 22, 23).

7.2 Stratified Sampling

Rather large initial cracks are expected to be needed to obtain failures within the lifetime of the RCP flywheel (~[ ] cycles). Hence, stratified sampling of crack size is used to guarantee that large cracks will be present in the Monte Carlo simulation without an excessive number of trials. For a given stratum, the range of crack sizes is specified [$(a_o)_{lo}$ to $(a_o)_{hi}$ and $(b_o\text{-}a_o)_{lo}$ to $(b_o\text{-}a_o)_{hi}$]. The probability of having a crack within this cell is known from the distributions of a_o and $b_o\text{-}a_o$, and the assumption of independence. Cracks are sampled from the stratum in accordance with the marginal distributions for that cell (which are known from the overall distributions of a_o and $b_o\text{-}a_o$. The probability of failure given a crack in that stratum is then the number of failures (F) divided by the number or trials (S). The stratification needs to cover all crack sizes that can result in failure within the lifetime, and results are summed over all cells. This is expressed as

$$P_f = \sum_{cells} \text{(probability of a crack in the cell)} \left[\frac{F}{S}\right]_{cell} \qquad (7\text{-}3)$$

One problem with stratification schemes is to know what crack sizes to include in the strata. To overcome this difficulty, FRAISE uses automated stratification, as described in the following. WinPRAISE uses a similar automated stratification (Reference 22).

a_o and $(b_o\text{-}a_o)$ are independent random variables (either random variable can be exponential or lognormal). Use these random variables to define a plane (x, y) of possible crack sizes. [The use of these variables makes it easy to define the marginal distributions and to compute the probability of a crack being in a given stratum (also referred to as a cell)].

The largest possible value of the crack size b is the thickness of the RCP flywheel, which is denoted as h. Since the analysis of quarter-elliptical cracks is restricted to initial cracks whose radial depth, a_o, is less than the axial length, b_o, then the largest possible value of a_o for a quarter-elliptical crack, is also h. For cracks with $b_o=h$, it is possible to have crack with $a_o>h$, but they will be through the thickness. The initial cracks will therefore be broken into two classes: (i) quarter-elliptical cracks with $a_o<b_o$ and $b_o<h$, and (ii) through cracks with $a_o>h$ and $b=h$.

Consider the a_o – $(b_o\text{-}a_o)$ plane depicted in Figure 7-1. For the category of quarter-elliptical cracks ($a_o<b_o$ and $b_o<h$), half of the plane is excluded.

The initial crack size plane containing possible cracks in this category (the lower triangle in Figure 7-1) is then broken up into strata. Consider stratification into *M* equal cells in the *x* direction (b_o - a_o) direction and *N* equal cells in the *y* direction (a_o) direction, as shown in Figure 7-2.

For ease of computation, the straight 45º line marking the edge of the excluded area is replaced by a stairstep so that each stratum sampled from is rectangular in a_o - (b_o - a_o) space. This is a good approximation as long as the *M* and *N* are not small.

It is also necessary to consider cracks that are initially through the thickness ($b_o > h$). These are expected to be of very low probability. For cracks in this category, the possible crack sizes are broken up into steps of Δa. This is depicted in Figure 7-3.

In this case, the probability of having a crack in the "cell" is defined from only the distribution of *a*, and the marginal distribution for a "cell" is also defined by the distribution of *a*. Cracks are sampled from each increment of *a*, and the probability of failure given a crack in that increment is evaluated by Monte Carlo.

The stratification is automated by specifying the following:

number of cells in the *s* direction, *M*

number of cells in the *a* direction, *N*

maximum number of samples in each cell, *S*

truncation, *T*.

Appropriate values to use depend on the problem, as is discussed in Section 8.

The a_o-(b_o-a_o) plane is broken up into cells as shown in Figure 7-2. For a given cell, samples of crack sizes are drawn from the marginal distributions for that cell, up to a maximum number, *S*. Samples are drawn for a given cell until S have been drawn, or F failures occur within the horizon time. Sampling in that cell is then stopped. The probability of failure given a crack in the cell is

$$P_{f.cell} = \frac{F}{S} \tag{7-4}$$

(If inspections take place, the number of failures is replaced by the sum of the indicator functions).

The sampling then proceeds to the next cell.

The whole sampling scheme begins at the longest and deepest (part-through) crack and proceeds to smaller cracks. Referring to Figure 7-2, the calculations start in the indicated cell. When either *F* failures occur or *S* samples have been drawn in that cell, the calculations proceed to the next cell. This would either be the next cell to the left, or down one row and adjacent to the exclusion line. In this way we are proceeding to progressively smaller cracks. This is continued until no failures occur in a cell, and also none in the next lower row in the cell against the exclusion line. This assures that no failures will occur in any unsampled cells – if only *S* samples are taken, so no sampling is performed from these cells. This can greatly reduce the computer time. Also, truncating the sampling at *T* can reduce the computer time; once we have *T* failures, we don't need to know much more about failures contributed by cracks in that cell.

Turning now to through cracks ($a_o>h$, $b=h$), Figure 7-3 is the counterpart of Figure 7-2, which is for part-through cracks. In this case the line for $a_o>h$, $b_o=h$ is broken into increments Δa. The probability of a crack in each step is obtainable from the distribution of a_o. If the probability of failure given an initial crack in the starting cell of Figure 7-2 is not close to 1, then Monte Carlo sampling steps up the increments in *a* until it does approach 1. Then the contributions from the through cracks are added up and included in the overall failure probability. If the probability of failure given a crack in the starting cell is close to 1, then the contribution of through cracks is the probability that $a_o>h$.

Once the probability of failure given a crack in each cell (that can contribute to failure), the overall probability of failure is obtained by use of Equation 7-2. This can proceed as a function of time (cycles).

7.3 Inspections

The influence of inspections is treated by use of "indicator functions". The nondetection probability, $P_{ND}(a)$, is the probability of not detecting a crack as a function of its size, *a*. This function is specified in FRAISE by a user-defined table. If a crack that has been inspected subsequently fails, this counts of P_{ND} failures, rather than 1 failure, where P_{ND} is evaluated at the value of *a* at the time of the inspection. Hence, rather than counting as one failure, it counts as P_{ND} failures. This is the procedure used in PRAISE (Reference 23).

If more than one prior inspection has taken place, the indicator function is the product of the P_{ND}s each evaluated at *a* at the time of the respective inspections. This takes credit for each inspection, and may over predict the benefit of successive inspections. Another way to treat successive inspections is to take the indicator function as the value of P_{ND} at the time of the last inspection prior to failure.

Considering all inspections and the product of the nondetection probabilities is termed independent, and using only the last P_{ND} is termed dependent inspections. Independence or dependence of inspections is specified by the user.

The following is a functional form that could be useful in generating a P_{ND} table.

$$P_{ND}(a) = \varepsilon + \frac{1}{2}(1-\varepsilon)\,\mathrm{erfc}\left[\upsilon \ln\frac{a}{a^*}\right] \qquad (7\text{-}5)$$

ε is the probability of not detecting a crack no matter how large it is,

a^* is the crack size having an approximately 50% chance of being detected, and

υ is a curve fit parameter that controls how abruptly the nondetection probability changes when a is close to a^*.

Equation 7-5 can be used to generate the P_{ND} table for input to FRAISE. Values of the parameters describing the probability of not detecting a crack [$P_{ND}(a)$] as a function of its size are given by Khaleel and Simonen (Reference 24, 25, 26) for various qualities of inspection; outstanding, very good, good and marginal. According to Khaleel (Reference 25), Pacific Northwest National Laboratory (PNNL) experts judge the qualities of the inspections according to the following categories:

marginal: A detection performance described by this curve would represent a team using given equipment and procedures that would have only a small chance of passing an Appendix VIII (of the ASME Boiler and Pressure Vessel Code) performance demonstration.

good: A detection performance described by this curve corresponds to the better performance levels in the PNNL round robin.

very good: This curve corresponds to a team with given equipment and procedures that significantly exceed the minimum level of performance needed to pass an Appendix VII performance test.

advanced: This curve describes a level of performance significantly better than expected from present-day teams, equipment and procedures that have passed an Appendix VIII-type of performance demonstration. (This performance level implies advanced technologies and/of improved procedures that could be developed in the future.)

The constants in Equation 7-5 for the nondetection probabilities are summarized in Table 7-3. The values of the constants are given by Simonen and Khaleel (Reference 24, 25, 26). Some are also in Reference 27.

Table 7-1: Summary of Random Variables in FRAISE

Description	Symbol	Distribution Type	Note
crack depth	a_o	lognormal or exponential	
crack length	b_o-a_o		b_o is crack length, (b_o-a_o) independent of a_o
fatigue crack growth coefficient	C	lognormal	
fatigue crack threshold	ΔK_{th}	lognormal	
fracture toughness	K_{Ic}	three-parameter Weibull	depends on RT_{NDT}
RT_{NDT}	RT_{NDT}	normal	
max speed during transient		normal	
temperature during transient		normal	
nondetection probability	$P_{ND}(a)$		user defined in table

Table 7-2: Distributions Considered in FRAISE

Name	Probability Density Function	Cumulative Distribution	Mean or Median	Other Parameters
Lognormal	$\frac{1}{\mu x\sqrt{2\pi}} e^{-\frac{1}{2\mu^2}\left[\ln\left(\frac{x}{x_{50}}\right)\right]^2}$	$\frac{1}{2}\,\mathrm{erfc}\left[\frac{\ln(x/x_{50})}{\mu\sqrt{2}}\right]$	median = x_{50}	μ =std dev(ln$x$)
Normal	$\frac{1}{\sigma\sqrt{2\pi}} e^{-\left[\frac{x-x_{50}}{\sigma\sqrt{2}}\right]^2}$	$\frac{1}{2}\,\mathrm{erfc}\left[\frac{x_{50}-x}{\sigma\sqrt{2}}\right]$	mean =median =x_{50}	std dev = σ
Exponential	$\frac{1}{b} e^{-x/b}$	$1-e^{-x/b}$	mean=b	--
3 Parameter Weibull	--	$P(x)=1-e^{-\left[\frac{x-x_o}{b}\right]^c}$ $P(x)=0$ if$x<x_o$	--	b, c, x_o

Table 7-3 Parameters of the Equation Describing the Non-Detection Probability of Inspections SCC

		Fatigue Cracks	SCC: Stress Corrosion Cracks
Outstanding (advanced)	*a*/h*	0.05	0.05
	ν	1.6	1.6
	ε	0.005	0.005
Very good	*a*/h*	0.15	0.15
	ν	1.6	1.6
	ε	0.02	0.02
Good	*a*/h*	--	0.40
	ν	--	1.6
	ε	--	0.10
Marginal	*a*/h*	0.4	0.65
	ν	1.6	1.4
	ε	0.1	0.25

h = wall thickness

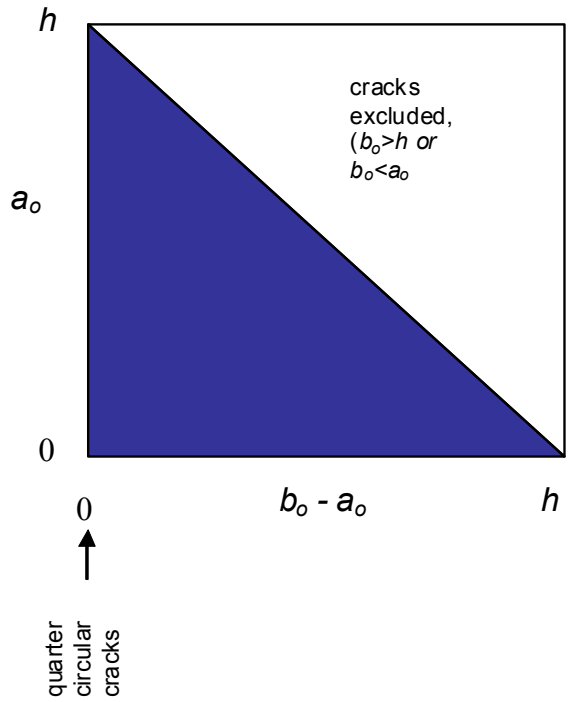

Figure 7-1 Initial Crack Size Plane Showing Region of Exclusion for Cracks with $a_o < b_o$ and $b_o < h$

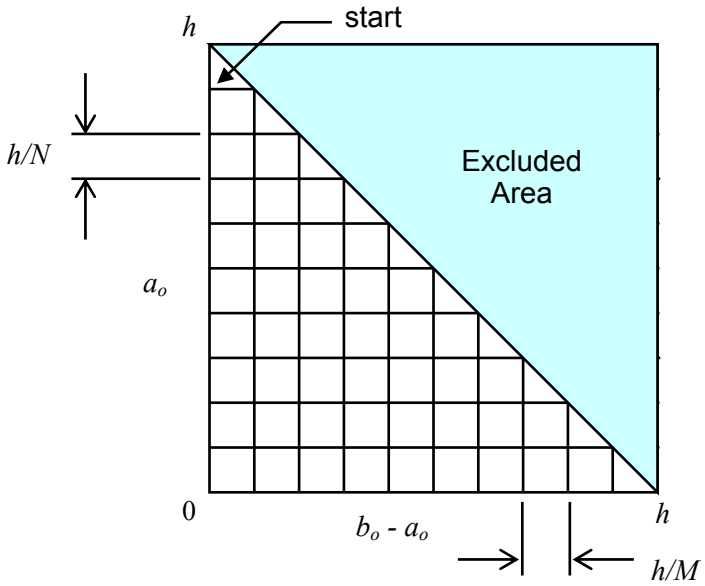

Figure 7-2 Initial Part-through Crack Size Plane Stratified into *M* x *N* Strata

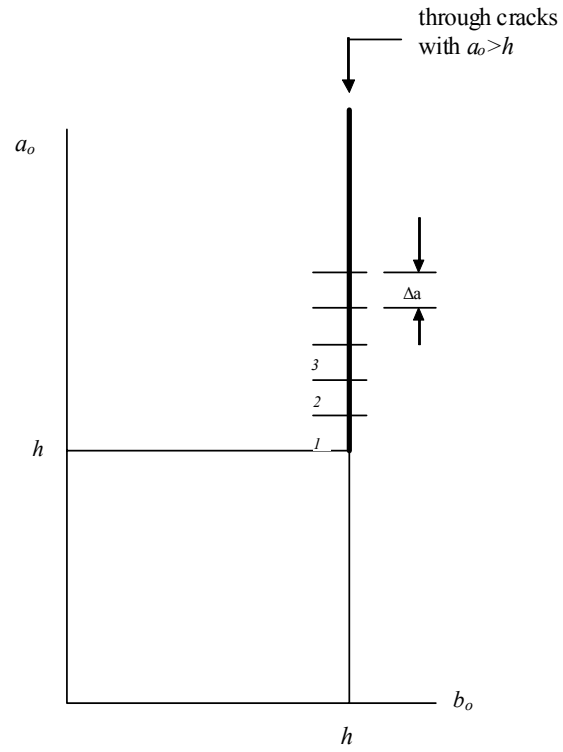

Figure 7-3 Initial Crack Size Plane for Through Cracks Showing Increments of a_o for Stratified Sampling

8.0 DEFINITION OF PROBLEMS

The purpose of this study is to investigate the influence of ISI on the reliability of RCP flywheels. To accomplish this, the FRAISE software is applied to the RCP flywheel shown in Figure 1-2, 1-3 and 2-1, with the operating conditions summarized in Table 1-1.

The speeds shown in Table 1-1 are taken as the mean of a normal distribution, with the standard deviation equal to [ ] times the mean. The temperature is taken to have a mean of [ ] ºF and a standard deviation of [ ] ºF. Hence, the lower part of Table 1-1 is expanded to appear as in Table 8-1.

As shown in Table 1-1, the overspeeds occur from 1200 to 1500RPM, so the fatigue history is equivalent to [ ] times to 1500 RPM and ([ ]) cycles of normal operation to 1200 RPM. The maximum RT_{NDT} in the material specification is reported to be 10 ºF as shown in the US-APWR DCD Section 5.4.1.1, and this temperature is fixed at this value in this analysis.

The following two inspection schedules are considered in plant operating years:

(i) Every 3 years (0, 3, 6, 9, 12, 15……54, 57)

(ii) Every 20 years (0, 20, 40)

Two inspection detection probabilities are considered, a good inspection and a not-so-good inspection. All inspections are taken to be independent (See Section 7.3). In order to estimate a set of detection probabilities, Equation 7-5 is employed, along with guidance from Table 7-3 and results included in Figure 8-1 (Reference 28).

Figure 8-1 shows a crack length of 0.040 inch as having about a 50% chance of being detected, except for the X-ray results. Table 7-3 shows all vales of a^* to scale with thickness, but these values are for piping inspections, whereas the cracked location of the RCP flywheel to be inspected is readily accessible and buried cracks are not of concern. Hence, the value of a^* is believed to not scale with the thickness in the RCP flywheel case. Hence, the 0.040 inch value will be taken to be applicable to a “good” inspection. This will be increased to 0.20 inch for a “not-so-good” inspection. Figure 8-1 shows this to be a very conservative value, except for the case of the X-ray.

Table 7-3 shows nearly all cases to have a value ν of 1.6, and this value is assumed here.

The value of ε (probability of not detecting a crack no matter how large it is) will be taken to be 0.005 for a “good” inspection and 0.02 for a “not-so-good” inspection. These values are consistent with values in Table 7-3 and Figure 8-1.

Selected points along the line in Figure 8-1 for the penetrant testing (PT) were digitized and plotted along with predictions using the “good” and “not-so-good” parameters along with Equation 7-5. The results are shown in Figure 8-2, which is on lognormal probability scales.

This figure shows good agreement between the “good” inspection and the digitized data points from the line in Figure 8-1 for PT, and that the “not so good” detection probabilities are much less favorable.

Four problems have been defined for the study of the influence of ISI. They will be designated as summarized in Table 8-2.

Calculations were performed on a print-interval by print-interval basis, with a print interval of 1 year.

The Monte Carlo stratification was selected by performing a study of effect of the scheme on the result. Too few samples provide results that change in successive runs. Too many samples results in excessive run time. Table 8-3 summarizes the results of the study on stratification schemes. The ‘not-so-good’ 20 problem was concentrated upon, with the other cases in Table 8-2 also considered. In some instances, the seed of the random numbers was fixed, as indicated by a check mark in Table 8-3. The following convention is used in the stratification identification in Table 8-3.

Strata in b_o-a_o	Strata in a_o	Samples per Stratum	Truncation
40	40	20k	50

Table 8-3 shows that the replicate results for a given stratification scheme are quite close to one another, but the values change significantly when the stratification scheme is changed. However, computer execution time increases rapidly as more strata are used.

In order to assure that the results have converged, an analysis was performed for only the overspeed transient, for minimal cycling and no inspection. This reduced the execution time. The speed was fixed at 1500 RPM and the temperature fixed at [ ] ºF. The results in Table 8-4 were obtained.

The results of Table 8-4 should serve as an upper bound, because no inspection is considered. Alternatively, the RPM and temperature have been fixed in Table 8-4, but not in Table 8-3.

Figure 8-3 summarizes the results of the stratification scheme study.

Figure 8-3 shows the increase in failure probability as the stratification is made finer, but shows the results leveling out. The figure also shows that the scatter in results of replicate runs. The results level out at values within the range of the overspeed results, thereby indicating that further refinement of the stratification will not significantly change the results.

Based on the above results, the following stratification scheme is selected as a compromise between accuracy and execution time.

strata in b_o-a_o = 60

strata in a_o = 100

samples per statum = 20,000

truncation of sampling = 50

The stratification of initially through-wall cracks does not significantly affect the results, because such large cracks are present only with a very small probability.

Another conclusion drawn from the results shown in Table 8-3 is that the difference between replicate runs is considerably larger than the difference between the 3 and 20 year inspection interval. Hence, in order to isolate the affect of inspection, the study of inspection is conducted with a fixed random number seed.

Table 8-1 RCP Flywheel Operating Conditions

	RPM			Temperature	
	Mean	Standard Deviation	Number (60 yrs)	Mean	Standard Deviation
Normal Operation	1200				
Overspeed	1500				

Table 8-2 Designation of the Four Problems in the Study of Influence of ISI

		Inspection Schedule	
		3 yrs	20 yrs
Detection Probability	Good	G3	G20
	Not So Good	NSG3	NSG20

Table 8-3 Results of Study of Monte Carlo Stratification Study 10^{12} (Cumulative Failure Probability in 60 years) (unshaded cells are replicate results)

ID	det	t_I	Fix Seed	40, 40 5k, 30	40, 40 20k, 50	60, 100 20k, 50
a	NSG	20	✓			
b	G	20	✓			
c	NSG	3	✓			
d	G	3	✓			
e	NSG	20				
f	NSG	20				
g	NSG	20				
h	NSG	20				

Note:

The shaded cells are related to the affects of inspection, and are discussed in detail in Section 9.

Table 8-4 Results for Only Overspeed, No Inspection

Stratification	10^{12} P_f	Exec Time
80,80,20k,100		
80,80,20k,100		
101,200,20k,100		
101,200,20k,100		

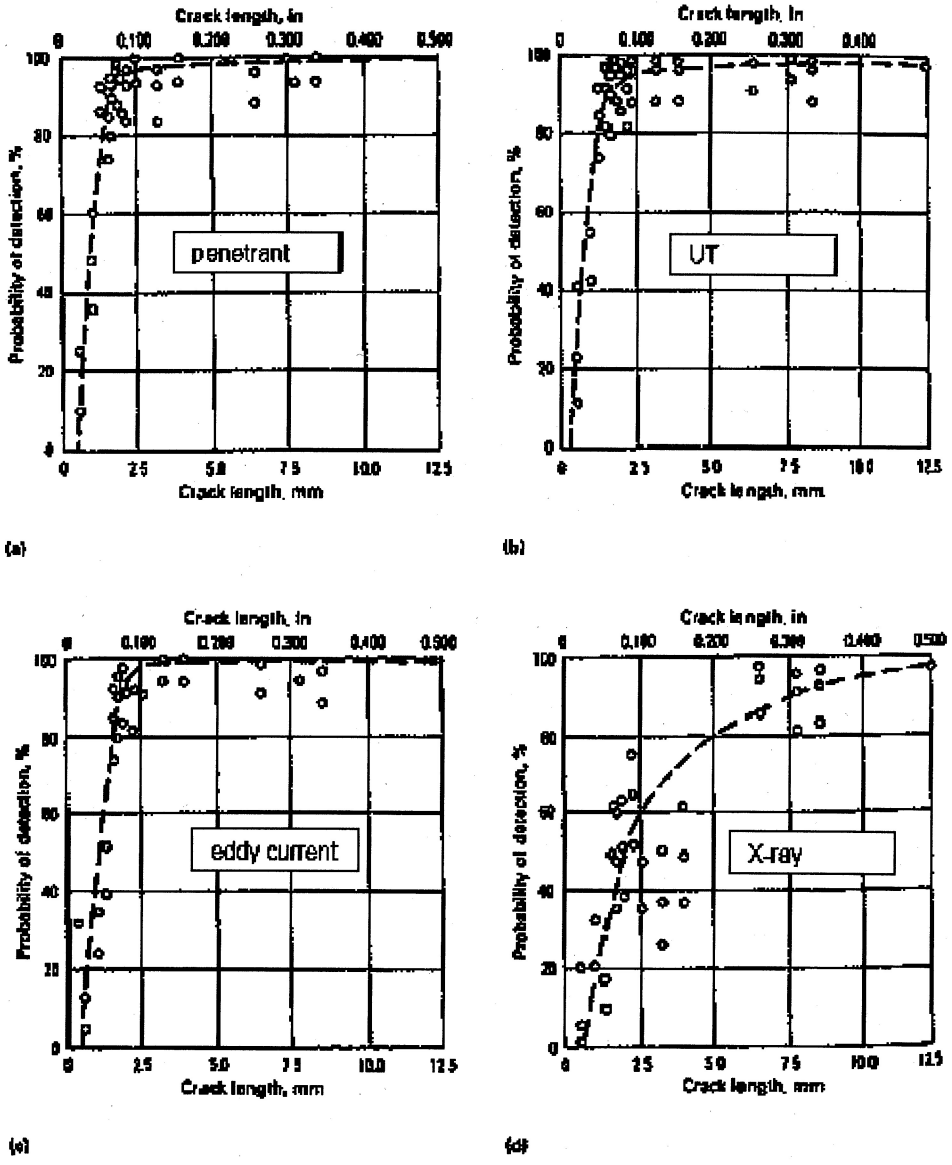

Figure 8-1 Probability Detection Probability for Four Inspection Methods on the Same Set of Specimens

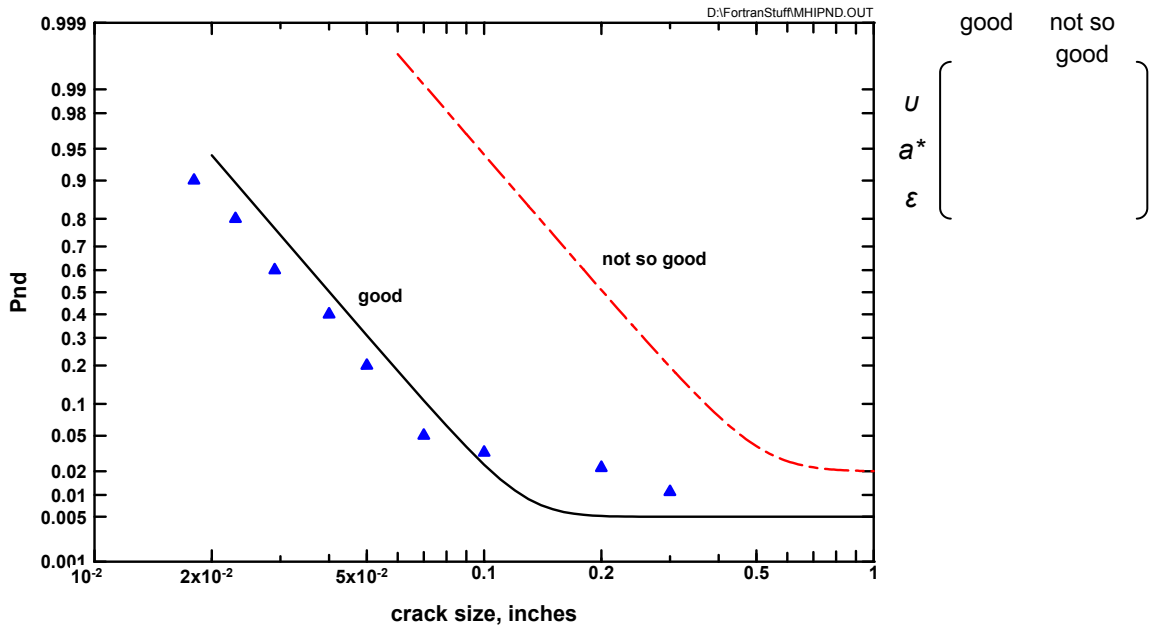

Figure 8-2: Non-detection Probability as a Function of Crack Size for PT

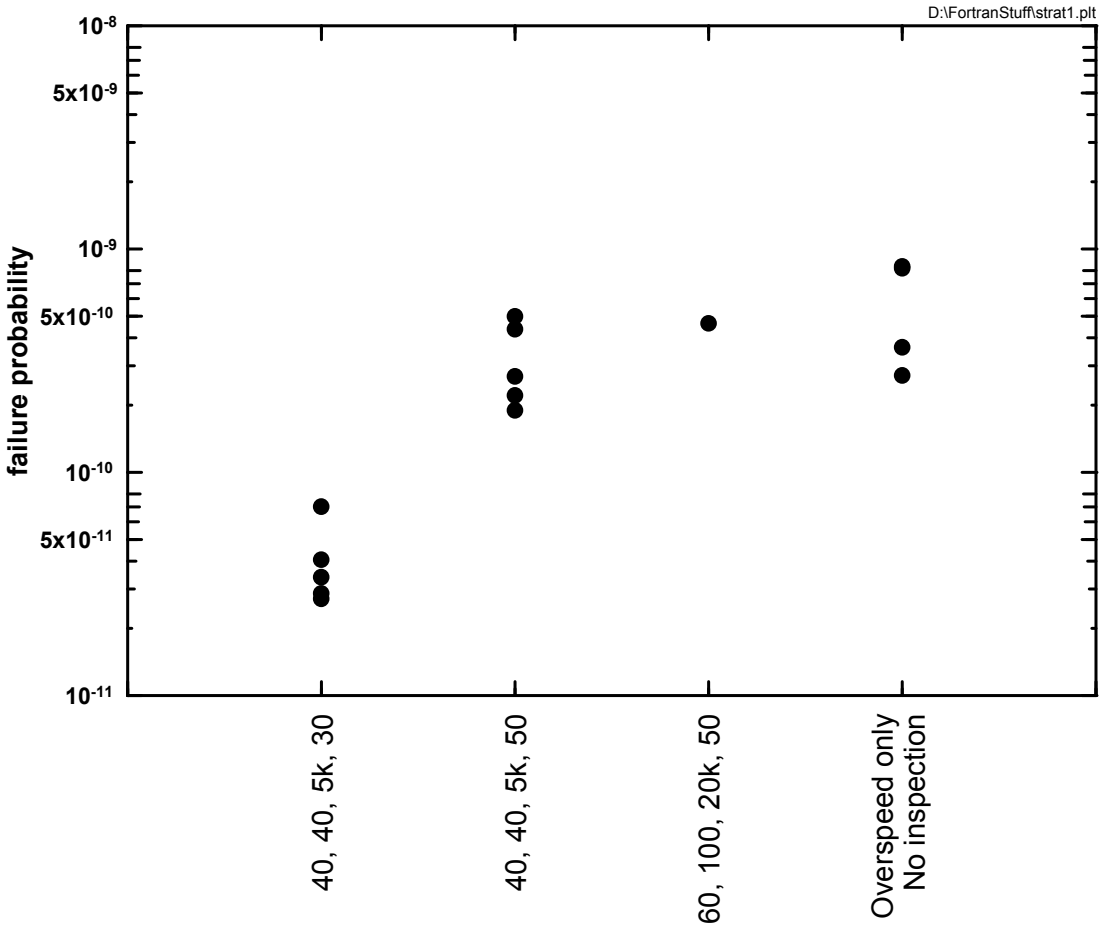

Figure 8-3 Summary of Results of Stratification Study

9.0 RESULTS

The results of the study of inspection detection probability and interval are summarized in this section. The four problems summarized in Table 8-2 are analyzed; that is, 3 and 20 year inspection intervals are considered with a “good” and “not so good” detection probability. All inspections are taken to be independent. In order to isolate the affect of inspection, and eliminate inaccuracies due to finite sampling, all these runs were made with the same fixed random number seed. As outlined at the end of Section 9, the stratification scheme was

strata in b_o-a_o = 60

strata in a_o = 100

samples per statum = 20,000

truncation of sampling = 50.

Table 9-1 provides the results, which are also included in Figure 9-1.

The results of Table 9-1 and Figure 9-1 show that the computed failure probabilities are invariably very small, and are affected by the quality of the inspection, but not the frequency of inspection. That is, the pre-service inspection (PSI) has a large affect, but the frequency of later ISI has only a small influence. The results show an abrupt jump following year 1, which is because the first overspeed occurs in the second year (1/f = 1/0.5833 = 1.71 years). The failure probability does not change much with time after the first overspeed, which means that minimal fatigue crack growth takes place. If the RCP flywheel survives the first overspeed, it is very unlikely to fail in later service.

The difference in the failure probabilities for a 3 and a 20 year inspection interval is negligibly small, indicating that the change from the RG1.14 (Reference 1) required inspection interval from 40 months to 20 years should not increase risk due to failure of the RCP flywheel.

Table 9-1: Summary of Results of Inspection Study Problems

	Not-So-Good Inspection	Good Inspection	Not-So-Good Inspection	Good Inspection
	Every 20 years	Every 20years	Every 3 years	Every 3 years
t	NSG20	G20	NSG3	G3
yrs	a	b	c	d
1				
2				
3				
4				
5				
6				
7				
8				
9				
10				
11				
12				
13				
14				
15				
16				
17				
18				
19				
20				
21				
22				
23				
24				
25				
26				
27				
28				
29				
30				
31				
32				
33				
34				
35				
36				
37				
38				
39				
40				
41				
42				
43				
44				
45				
46				
47				
48				
49				
50				
51				
52				
53				
54				
55				
56				
57				
58				
59				
60				

Figure 9-1 Cumulative Failure Probability as a Function of Time for Different Inspection Schedules and Detection Probabilities

10.0 SUMMARY AND CONCLUSIONS

A study of the influence of in-service inspection on the reliability of a RCP flywheel has been performed using a PFM model of the growth and criticality of pre-existing defects. The random variables considered in the model are

- Initial crack depth, a_o
- Initial crack length, b_o (actually b_o-a_o)
- Reference nil ductility temperature, RT_{NDT}
- Fracture toughness, K_{Ic}
- Operating speed
- Operating temperature
- Fatigue crack growth rate (for a given minimum and maximum stress intensity factor)
- Fatigue crack growth threshold

The statistical distributions of the material-related random variables were estimated from the literature.

The probabilistic model utilizes Monte Carlo simulation, with stratified sampling of crack sizes. Using the FRAISE code and operating conditions of the RCP flywheel, the computed failure probabilities were determined to be invariably very small; (on the order of [ ] cumulative in 60 years). After the first overspeed transient, the failure probabilities did not increase appreciably with time, thereby indicating that fatigue crack growth is not a contributor to the failures.

A study of the influence of inspection quality and frequency was performed. Inspections every 3 and 20 years (3 years ~ 40 months) were considered, including a PSI. A “good” and a “not-so-good” detection probability were considered. It was found that the quality of the inspection was important, but the inspection frequency was not. After the first overspeed (at 1.71 years) the computed failure probability did not increase noticeably with time no matter what ISI interval was considered. This is because if failure was to occur during an overspeed, it is most likely to occur the first time. Failure is much less likely on the second and subsequent overspeeds.

These results suggest that a good PSI is very beneficial, and that a pre-service overspeed would be effective in reducing the probability of failure in service, but that successive ISI are not instrumental in reducing failures due to the growth and instability of pre-existing defects.

The results of this study therefore indicate that a 20 year inspection interval following the PSI is justified in lieu of the RG 1.14 (Reference 1) required inspection interval of 40 months. The increased risk due to failure of the RCP flywheel with the 20 year inspection interval is negligibly small.

11.0 REFERENCES

1. Reactor Coolant Pump Flywheel Integrity, Regulatory Guide 1.14, Rev.1, U.S. Nuclear Regulatory Commision, Washington DC, August 1975.

2. ASME Boiler and Pressure Vessel Code, Section XI. 2004 Edition, American Society of Mechanical Engineers

3. Acceptance for Reference of Topical Report WCAP-14535, Topical Report on Reactor Coolant Pump Flywheel Inspection Elimination, U.S. Nuclear Regulatory Commission letter from Brian W. Sheron to Sushil C. Jain (Duquesne Light Company), September 12 1996.

4. Acceptance for Referencing Topical Report SIR-94-080 – Relaxation of Reactor Coolant Flywheel Inspection Requirement, U.S. Nuclear Regulatory Commission letter from Brian W. Sheron to Dwight C. Mims (ANO-Entergy Operations), May 21, 1997.

5. Theory of Elasticity, S.P. Timoshenko and J. N. Goodier, McGraw-Hill Book Co., New York, 1951

6. ANSYS, Release 11.0, ANSYS,Inc., Canonsburg, PA, 2007

7. Stress Analysis of Cracks Handbook, H. Tada, P.C. Paris and G.R. Irwin, ASME Press, New York, 2000

8. MATHCAD, MathSoft, Cambridge, Massachusetts

9. pc-CRACK, Version 4.0 (Beta Release 0.024), Structural Integrity Associates, San Jose, California, 2009

10. Stress Intensity Factors and Weight Functions for a Corner Crack in a Finite Thickness Plate, X.J. Zheng, G. Glinka and R.N. Dubey, Engineering Fracture Mechanics, Vol. 54, No. 1, 1997, pp. 49-61

11. Stress-Intensity Factors for Small Surface and Corner Cracks in Plates, I.S. Raju, S.N. Atluri and J.C. Newman, Jr., Fracture Mechanics: Perspectives and Directions, ASTM STP 1020, 1989, pp. 297-316

12. A Generalized Procedure for Generating Flaw-Related Inputs for the FAVOR Code, Simonen, F. A., S. R. Doctor, G. J. Schuster, and P. G. Heasler, NUREG/CR-6817, U.S. Nuclear Regulatory Commission, October 2003

13. Application of Statistically-Based K_{Ic}/K_{Ia} Fracture Toughness Models to PTS Assessment of Reactor Pressure Vessels, B. R. Bass, T. L. Dickson, P. T. Williams, ORNL/NRC/LTR-00/02, April 2000

14. Nuclear Pressure Vessel Steel Data Base, W.L. Server and W. Oldfield, Electric Power Research Institute Report NP-933, 1978

15. Technical Basis for a Revised Fatigue Crack Growth Rate Reference Curve for Ferritic Steels in Air, E.D. Eason, J.D. Gilman, D.P. Jones and S.P. Andrew, Journal of Pressure Vessel Technology, Vol. 114, February 1992, pp. 80-86

16. Extensive Study of Low Temperature Fatigue Crack Growth Rates in A533 and A508 Steels, P.C. Paris, R.J. Bucci, E.T. Wessel, W.G. Clark and T.R. Mager, Stress Analysis and Growth of Cracks, Proceedings of the 1971 National Symposium on Fracture Mechanics, Part I, ASTM STP 513, 1972, pp. 141-176

17. The Influence of Load Ratio and Temperature on the Near-Threshold Fatigue Crack Growth Properties of Pressure Vessel Steels, P.K. Liaw and W.A. Logsdon, Journal of Engineering Materials and Technology, ASME, Vol. 107, 1985, pp. 107-33

18. Probability Concepts in Engineering Planning and Design, Vol. I: Basic Principles, A.H.-S. Ang and W.H. Tang, John Wiley & Sons, New York, 1975

19. Handbook of Mathematical Functions, National Bureau of Standards Applied Mathematics Series 55, M. Abramowitz and I. Stegun, Washington, DC, 1964

20. Probability of Pipe Fracture in the Primary Coolant Loop of a PWR Plant, Vol. 5: Probabilistic Fracture Mechanics Analysis, D.O. Harris, E.Y. Lim, and D.D. Dedhia, NUREG/CR–2189, Vol. 5, U.S. Nuclear Regulatory Commission, Washington, DC, August 1981

21. Theoretical and User's Manual for pc-PRAISE, A Probabilistic Fracture Mechanics Code for Piping Reliability Analysis, D. O. Harris, D. Dedhia and S. C. Lu, NUREG/CR-5864, U.S. Nuclear Regulatory Commission, Washington, D.C., July 1992

22. WinPRAISE 07: Expanded PRAISE Code in Windows, Structural Integrity Associates, San Jose, California, 2007

23. Probability of Pipe Fracture in the Primary Coolant Loop, of a PWR Plant, Vol. 9: PRAISE Computer Code User's Manual, E.Y. Lim, NUREG/CR-2189, Vol. 9, U.S. Nuclear Regulatory Commission, Washington, DC, August 1981

24. The Effects of Initial Flaw Size and Inservice Inspection on Piping Reliability, M.A. Khaleel and F.A. Simonen, Service Experience and Reliability Improvement: Nuclear, Fossil, and Petrochemical Plants, ASME PVP-Vol.288, 1994, pp. 95-107

25. The Impact of Inspection on Intergranular Stress Corrosion Cracking for Stainless Steel Piping, M.A. Khaleel, F.A Simonen, D.O. Harris and D. Dedhia, Risk and Safety Assessment: Where is the Balance?, ASME PVP-Vol.296/SERA-Vol.3, 1995, pp. 411-422

26. Effects of Alternative Inspection Strategies on Piping Reliability, M.A. Khaleel and F.A. Simonen, Fatigue and Fracture – 1997, Vol. 2, ASME PVP-Vol. 346, 1997, pp. 207-215

27. Technical Elements of Risk-Informed In-service Inspection Programs for Piping, Draft Report, NUREG-1661, U.S. Nuclear Regulatory Commission, Washington, DC, January 1999

28. Applications of NDE Reliability to Systems, W.D. Rummel, G.L. Hardy and T.D. Cooper, Metals Handbook, Vol. 17, Nondestructive Evaluation and Quality Control, 9th Edition, ASM International, Metals Park, Ohio, 1989, pp. 674-688